國立臺灣大學工學院應用力學研究所

碩士論文

Institute of Applied Mechanics

College of Engineering

National Taiwan University

Master's Thesis

通過腦組織脈動估算大腦性質

Estimating Cerebral Properties via Brain Tissue Pulsations

毛宇真

Yu-Zhen Mao

指導教授：潘斯文 博士

Advisor: Stephen Payne, Ph.D.

中華民國 113 年 7 月

July, 2024

doi:10.6342/NTU202403075

Acknowledgements

I want to express my deepest gratitude to my advisor, Professor Stephen Payne, for his unwavering support throughout my research. His insightful suggestions and timely interventions have been invaluable, especially during challenging times when I felt stuck. His vast knowledge has given me a solid foundation to tackle complex problems. Professor Payne's patience and understanding have allowed me to learn independently. His encouragement has helped me overcome obstacles and inspired me to push my boundaries and strive for excellence.

I am also immensely grateful to my lab mates, who have always supported me with my coding and math problems. Their willingness to share their knowledge and assistance has been crucial to my progress. I would also like to extend my heartfelt thanks to my parents for their unwavering support and encouragement. Their belief in my abilities and financial support has been the backbone of my journey. They have always been there for me, providing a stable and nurturing environment that has allowed me to focus on my studies and research.

Lastly, I want to thank everyone who has contributed to my academic journey. This acknowledgement is a small token of my appreciation for all you have done for me. Thank you.

doi:10.6342/NTU202403075

中文摘要

由於難以獲得無創的體內數據，理解腦組織的機械性質仍然具有挑戰性。本研究通過利用心臟周期引起的腦組織脈動（BTP）來估算腦部性質。研究開發了一個耦合固-液的數學模型，並使用經顱組織多普勒（TCTD）技術測量 20 名健康個體的腦組織位移和相應的血壓，從而獲得數據。傅里葉變換被用來推導位移和壓力信號之間的傳遞函數。

該數學模型假設腦組織可以被模擬為一個耦合固-液系統。球坐標系被應用於模型中以簡化控制方程。為了擬合數據，嘗試了兩種模型，包括耦合固-液模型及其具有多個組分的修正模型。使用 MATLAB 的'fminsearch'進行模型擬合，優化了包括楊氏模量（E）、泊松比（ν）、比儲量（Q）和透氣度/粘度（κ/μ）等關鍵參數。

總共嘗試了四種方法。前三種方法包括原始模型擬合、為避免負量級進行的對數變換模型擬合和修正模型擬合，這些方法擬合了由物理參數組成的無量綱參數組。然後，無量綱參數組可以計算出三個量綱參數。最後一種方法是直接擬合原始三個量綱參數，因為在無量綱參數組轉化為三個量綱參數的過程中存在問題。

擬合結果顯示所有方法的擬合曲線和損失都與實驗數據有很強的相關性。然而，參數值並不總是符合預期的量級。這種差異部分是由於缺乏已建立的比較標準。此外，這也間接表明了準確模擬腦組織性質的複雜性和挑戰性。

總結來說，雖然本研究沒有顯示出預期的結果，但仍然排除了幾種方法。儘管存在這些挑戰，本研究為利用腦組織脈動估算腦部性質的潛力和局限性提供了寶貴的見解。某些方法和模型的排除突顯了進一步改進模型以更好地考慮腦組織非線性、粘彈性和各向異性特性的必要性。該研究的方法還顯示出使用無創技術準確估算腦組織機械性質的潛力。未來的研究應該著重於通過引入更多數據集來提高這些模型的準確性，不僅包括健康志願者，還包括患者，以獲得更準確的結果。此外，未來的研究應該探索其他可能的建模技術。通過解決本研究中識別的局限性，研究人員可以提高無創方法估算腦組織性質的可靠性。此外，將這種方法擴展到各種生理和病理狀態，以增強其臨床應用性，特別是在診斷和治療腦部疾病方面，也將是重點。

關鍵詞：腦組織脈動，經顱組織多普勒，機械性質，無創技術，腦部性質估算，臨床應用，耦合固-液數學建模

doi:10.6342/NTU202403075

Abstract

Understanding the mechanical properties of brain tissue remains challenging due to difficulties obtaining non-invasive in vivo data. This study addresses this by utilising brain tissue pulsations (BTP) from cardiac cycles to estimate cerebral properties. This study developed a coupled solid-fluid mathematical model fitted to data from 20 healthy individuals using Transcranial Tissue Doppler (TCTD) to measure brain tissue displacement and corresponding blood pressure. The Fourier transformation was used to derive transfer functions between displacement and pressure signals.

The mathematical model assumes that the brain tissue can be modelled as a coupled solid-fluid system. The spherical coordinate is applied to the model to simplify the governing equation. Two models have been tried to fit the data, including a coupled solid-fluid model and its revised model with multiple compartments. Model fitting, using MATLAB's 'fminsearch,' optimised vital parameters, including Young's modulus (E), Poisson's ratio (ν), specific storage (Q), and permeability over viscosity (κ/μ).

Four ways are tried in total. The first three, including original model fitting, logarithmic transformation model fitting to avoid negative magnitude, and revised model fitting, are fitting the non-dimensional groups of parameters formed by physical parameters. Then, the dimensional three can be calculated by non-dimensional groups. The last way is to directly fit the original dimensional three because problems exist from non-dimensional groups to the original three parameters.

The fitting results correlate with experimental data across all methods according to the fitting curves and loss. However, the parameter values don't always perform well with expected magnitudes. This discrepancy is partly due to the absence of established

doi:10.6342/NTU202403075

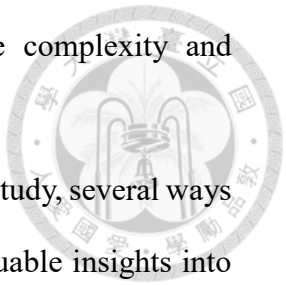

standards for comparison. This also indirectly demonstrates the complexity and challenging nature of accurately modelling brain tissue properties.

In conclusion, although an expected result hasn't been shown in this study, several ways are still excluded. Despite these challenges, this study provides valuable insights into the potential and limitations of using brain tissue pulsations for estimating cerebral properties. The exclusion of certain methods and models underscores the need for further refinement of more models that can better account for the nonlinear, viscoelastic, and anisotropic nature of brain tissue. This study's approach also shows the potential for using non-invasive techniques to estimate brain tissue's mechanical properties accurately.

Future research should focus on enhancing the accuracy of these models by incorporating more datasets, not only for healthy volunteers but also for patients, to get more accurate results. Also, future research should explore other possible modelling techniques. By addressing the limitations identified in this study, researchers can improve the reliability of non-invasive methods for estimating brain tissue properties. Besides, extending this methodology to various physiological and pathological states to enhance its clinical applicability, particularly in diagnosing and treating brain disorders, will also be a focus.

Keywords: Brain Tissue Pulsation(BTP), Transcranial Tissue Doppler(TCTD), Mechanical Properties, Non-invasive Techniques, Cerebral Properties Estimation Clinical applications, Coupled solid-fluid Mathematical Modeling

doi:10.6342/NTU202403075

Table of Contents

doi:10.6342/NTU202403075

doi:10.6342/NTU202403075

doi:10.6342/NTU202403075

圖次

doi:10.6342/NTU202403075

doi:10.6342/NTU202403075

doi:10.6342/NTU202403075

表次

doi:10.6342/NTU202403075

1 Introduction

There remains a surprising lack of understanding regarding the mechanical properties of brain tissue. Therefore, this study uses a non-invasive detection method called transcranial tissue Doppler (TCTD) to acquire brain tissue pulsation (BTP) data. This technique, which measures the movement of brain tissue using ultrasound waves, allows us to study the brain non-invasively in vivo. Although the existing methods, such as CT and MRI, can be used to infer many properties of the brain, there still are disadvantages, such as not quickly considering mechanical properties.

This study uses brain tissue displacement and blood pressure caused by cardiac pulsations, getting information to estimate the brain's mechanical properties through analytical methods and mathematical models. Understanding these properties is of great significance for treating patients with brain diseases. Additionally, the findings aim to inform the design of better diagnostic tools and treatments for brain disorders, leading to improved healthcare outcomes.

1.1 Background

The mechanical characteristics of brain tissue in vivo still need to be more adequately

doi:10.6342/NTU202403075

understood. This is partly because measurements taken from tissue outside the body often fail to reflect in vivo conditions accurately and also due to the significant challenges in studying organs so effectively shielded by mechanical defences. However, these properties are crucial for comprehending how the brain reacts to mechanical forces, such as those experienced during trauma and swelling(oedema). Improved in situ characterisation of the brain's mechanical properties would immensely benefit such research. It would also facilitate the development of more precise models of these two pathophysiological processes and enhance the availability of quantitative data for diagnostic and therapeutic purposes.

1.2 **Literature review**

In order to better comprehend the illness and carry out this investigation, a multi-angle literature evaluation is carried out. This literature review thus synthesises three key areas of study: clinical, experimental, and mathematical modelling, aiming to thoroughly assess their application and development in disease diagnosis and therapy. Clinical research provides direct observations of pathology and treatment effects, while experimental research investigates the underlying principles of pathophysiology and interventions. Mathematical models offer precise tools for understanding complex biological systems and predicting therapeutic outcomes. Although these fields differ in

doi:10.6342/NTU202403075

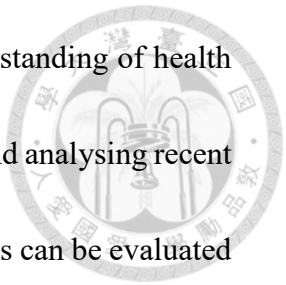

their research methods and focus, they all aim to advance the understanding of health and disease, propelling progress in medical science. By integrating and analysing recent research findings from these three areas, current therapeutic strategies can be evaluated more comprehensively. Also, data support and theoretical foundations will be provided for future research directions.

1.2.1 Clinical

The brain is known to pulse with every cardiac cycle, but only recently has there been interest in quantifying cardiac-induced brain tissue pulsations, or BTPs. [4]. Newborn infants originally found it by seeing through their fontanelle. Variations in the elasticity of brain tissue and the transmission of arterial pulses into adjacent tissue are thought to have a significant impact on the localized pulsations of brain tissue [4]. Brain Tissue Pulsations (BTP) hold significant potential for clinical applications. A systematic review [16] has summarised tissue pulsality imaging (TPI) research, indicating that Brain disease and impaired cerebral hemodynamics may be indicated by Brain Tissue Pulsations (BTPs) [4].

The cerebral vasculature is a huge and complex network of blood vessels that provide blood to all regions of the brain, facilitating the transportation of glucose and oxygen. [28]. The heartbeat is reflected in the pulsating blood flow that occurs in the brain

doi:10.6342/NTU202403075

arteries. This pulsatile nature of blood flow is crucial for maintaining the brain's metabolic demands and is characterised by periodic changes in velocity and pressure due to the heartbeat [28]. However, the effect of tissue ischemia, as a result of ischaemic stroke, on these brain tissue pulsations remains unclear [28].

In other words, while healthy brain tissue pulses in sync with the cardiac cycle, it is still uncertain if ischemic stroke impairs these pulsations due to tissue ischemia. [2]. According to the study done by Ince J et al. (2020), ischeamic stroke typically results from the blockage of major arteries that supply the brain and is the primary cause of death and disability globally. [1]. There is no suitable method for predicting strokes now. The stroke prediction methods available today rely on patient cooperation, take several minutes to complete, and are subjective. According to a recent systematic study, the average sensitivity and specificity of 19 stroke prediction measures were 80% and 68%, respectively[1]. Although brain imaging techniques exist, their performance is not exceptional. Early ischemia abnormalities are often not immediately evident on CT scans, and MRI scans can take up to 30 minutes to collect. These limitations affect the efficacy of CT and MRI to help in the early identification of stroke [1].

With the use of X-rays and computer processing, Computed Tomography (CT) is a medical imaging technique that produces incredibly detailed cross-sectional images of various body parts. CT scans offer more detailed visual representations of the internal

doi:10.6342/NTU202403075

structures compared to standard X-rays, making them ideal for quickly examining bones, muscles, fat, and organs to diagnose diseases, assess injuries, or plan surgeries. A circular X-ray machine passes through a motorized table that the patient rests on during a CT scan, taking pictures of the body from various angles. A computer then processes these images to produce visual slices, which can be further reconstructed into three-dimensional images. Due to its high resolution, CT is an indispensable diagnostic tool in modern healthcare.

Without using ionizing radiation, magnetic resonance imaging (MRI) is a non-invasive medical imaging method that creates high-resolution pictures of soft tissues. It operates by aligning hydrogen protons in the body with a strong magnetic field and using radiofrequency pulses to generate detected and processed signals into images. MRI excels in neurological, cardiovascular, musculoskeletal, and abdominal imaging due to its high resolution and ability to image in multiple planes. Despite its long scan times, high costs, and contraindications for patients with metal implants, MRI's detailed imaging capabilities and functional imaging options make it an indispensable tool in modern medicine.

Amplified MRI (aMRI) is a revolutionary technique introduced to enhance the visualization of pulsatile brain motion, making subtle physiological changes more noticeable. Initially developed in 2D formats, aMRI has been advanced into 3D

doi:10.6342/NTU202403075

technology that improves the detection and imaging of brain movements across all three spatial dimensions [3]. The 3D aMRI method provides superior image quality. It reduces motion artefacts compared to its 2D predecessor, offering more precise insights into the biomechanical behaviours of brain tissues influenced by cardiac pulsations and cerebrospinal fluid (CSF) dynamics [3].

The 3D aMRI utilises a phase-based motion magnification algorithm that amplifies the subtle motion within the brain, which is otherwise hard to detect with traditional imaging methods [3]. This technique is particularly useful for diagnosing and researching neurological diseases that affect the biomechanical properties of the brain and its fluids. By capturing brain movement in three dimensions, 3D aMRI offers a comprehensive view of the brain's biomechanical response, aiding in the understanding of disorders such as hydrocephalus and Chiari malformation, where altered brain motion is a key characteristic. [3].

In summary, When it comes to brain mobility, 3D aMRI provides better picture quality than 2D aMRI and can accommodate a larger amplification factor. The comparison of 2D aMRI and 3D aMRI is shown in Figure 1-1. The coronal image's optic chiasm area serves as a clear example of this, since brain motion there seems to be concentric rather than inferior or superior. 3D aMRI's optical flow maps and 4D animations may open up interesting new avenues for research into neurological conditions affecting the

doi:10.6342/NTU202403075

biomechanics and fluid dynamics of the brain [3].

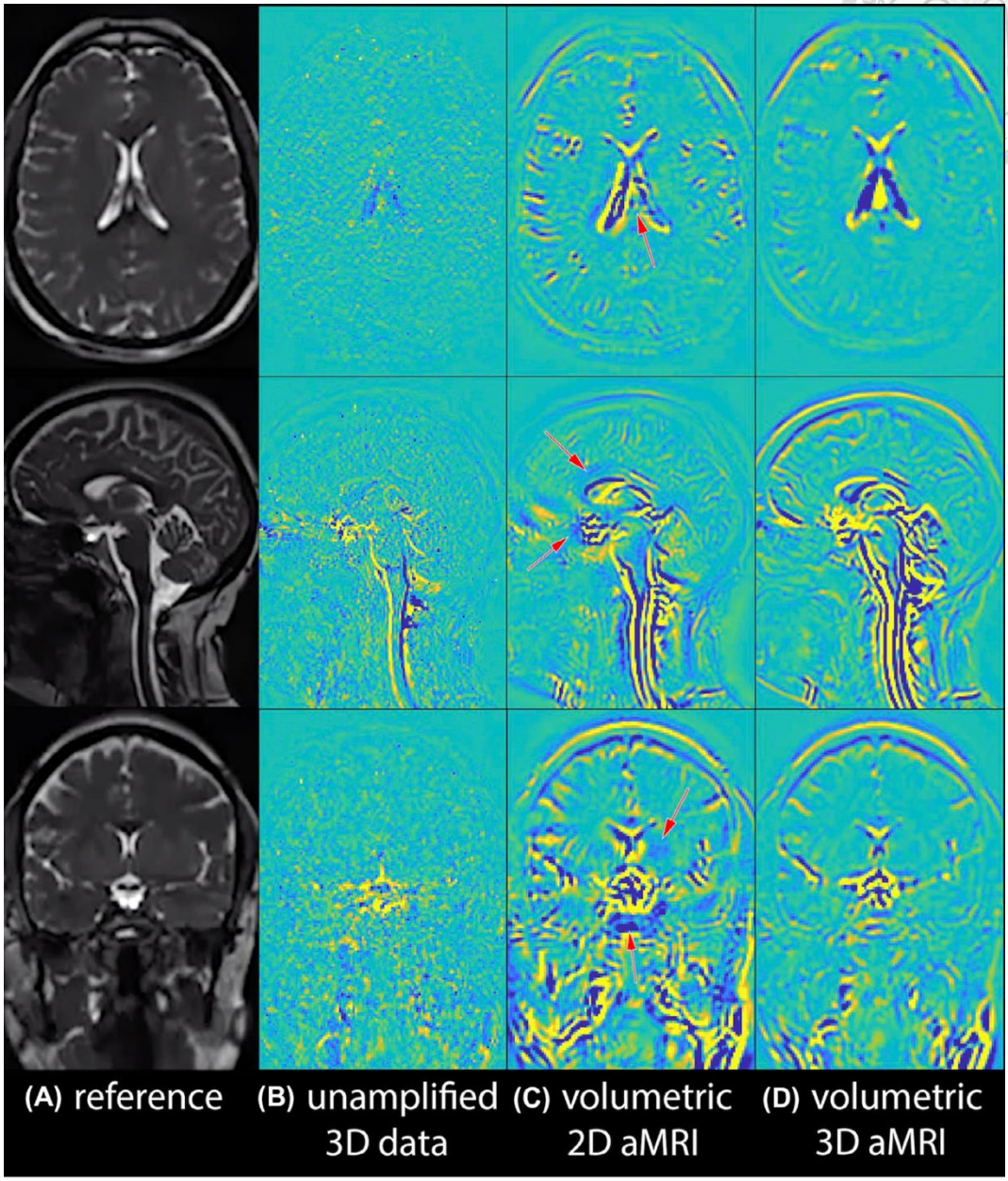

Figure 1-1 Comparing volumetric 2D and 3D aMRIs. Volumetric 2D aMRI (C), volumetric 3D aMRI (D), and original (unamplified) 3D cine data (B) were used to generate the maximum difference maps and the anatomical reference (A). When compared to volumetric 2D aMRI, volumetric 3D aMRI was able to capture both in- and out-of-plane motion with a considerable reduction in motion artifacts. [3].

This study intends to give the first estimations of brain tissue motion for a broad cross-section of healthy people for a literature review of brain tissue pulsations (BTP) [4].

doi:10.6342/NTU202403075

Turner P et al.(2020) first point out that the brain visibly pulsates in sync with the cardiac cycle in newborn infants and patients undergoing neurosurgery. Variations in brain tissue compliance and the spread of artery pulsations into the surrounding tissue are thought to have a major impact on the regional pulsations of brain tissue. [4]. Despite the long-standing use of Doppler techniques for assessing cardiac tissue motion, the use of Doppler ultrasound for measuring brain tissue motion is still largely uncharted. [4]. It is worth noting that this study also mentioned the amplified MRI (aMRI) and the relative study using this method. However, transcranial tissue Doppler (TCTD) is an innovative method that doesn't necessitate a skilled operator, utilizing a compact, wearable, single-element ultrasound probe. Besides, measurement can be obtained from any position on the head through this method [4].

Case study

Brain tissue pulsations (BTPs) were measured in 24 healthy volunteers (aged 52–82) and 14 acute ischemic stroke patients (aged 51–86) using a unique Transcranial Tissue Doppler (TCTD) technique. All of the participants tolerated the measures well, and they were completed quickly. [1].

The concept of measuring BTP by using Transcranial Tissue Doppler (TCTD) is because of its advantages, such as it doesn't necessitate a skilled operator, utilizing a

doi:10.6342/NTU202403075

compact, wearable, single-element ultrasound probe. This is the first study to examine if brain tissue pulsations (BTPs) are influenced by impaired tissue perfusion related to stroke, mainly ischemic one. [1]. A "plethysmography-based" process, in which the amount of arterial blood that enters the brain during systole surpasses the amount of venous outflow, has been proposed by some researchers as the cause of brain tissue pulsations (BTP). It is thought that with each cardiac cycle, the buildup of blood volume causes a modest but noticeable contraction of the volume of the brain [5].

Expanding the brain will generate and be increased in intracranial pressure during the cardiac cycle due to the skull's constant capacity. According to a 2007 supposition by J.C. Kucewicz et al., the pressure-volume balance among compartments of the brain may be relieved by the brain's descent through the foramen magnum and the consequent displacement of cerebrospinal fluid (CSF) into the spinal canal. Another detailed description is that brain tissue pulsations (BTPs) primarily result from the main arteries' pulsations spreading into the delicate brain tissue around them. [5].

However, both hypotheses are still under investigation. Ince J et al. (2020) compared brain tissue pulsations (BTPs) from stroke patients to the control subjects who had not had a stroke using a mixed methods technique. Their work provides an initial evaluation of the usefulness of Transcranial Tissue Doppler (TCTD) scans for the diagnosis of acute ischemic stroke. [1].

doi:10.6342/NTU202403075

1.2.2 Experimental

Ince J et al. (2020) used a conventional 2 MHz probe and a portable transcranial Doppler ultrasonography device from Spencer Technologies to record all brain tissue pulsation (BTP) readings. Because the left side of the forehead is easier to access in an emergency, recordings were made from both sides. [1].

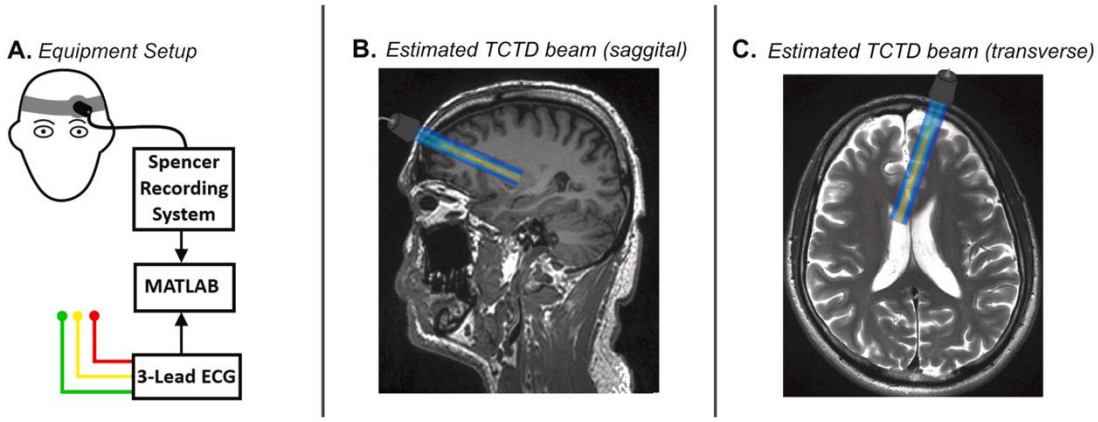

Figure 1-2 Acquisition of BTP. The predicted TCTD beam from side view (B) and top view (C) correspond to the equipment configuration (A). The forehead was the site of the probe, which was placed about 1 cm above the eyebrow's center. [1]

Using this technique, Ince J et al. (2020) examined the tissue displacement for 30 depths (ranging from 2 to 8 cm) inside the brain, with the data shown in MATLAB. [1]. This study included 14 acute ischaemic stroke patients and 24 non-stroke volunteers [1]. The non-stroke brain tissue pulsation and typical stroke brain tissue pulsation to the time in different depths are shown in Figure 1-3 and Figure 1-4. Figure 1-4 shows 4 features to identify recordings from stroke patients.

By comparing the signals between stroke and non-stroke signals, it was found that non-

doi:10.6342/NTU202403075

stroke signals exhibited higher consistency and typical features, such as quickly peaking after the start of the cardiac cycle followed by a rapid return to baseline. In contrast, stroke patients' BTP waveforms showed significant abnormal characteristics, such as severe waveform disruption and multiple additional peaks [1]. To explain why individual brain tissue pulsations (BTPs) differ, however, a much deeper understanding of the relationships between physiological changes, tissue biomechanics, and BTPs is necessary. [1].

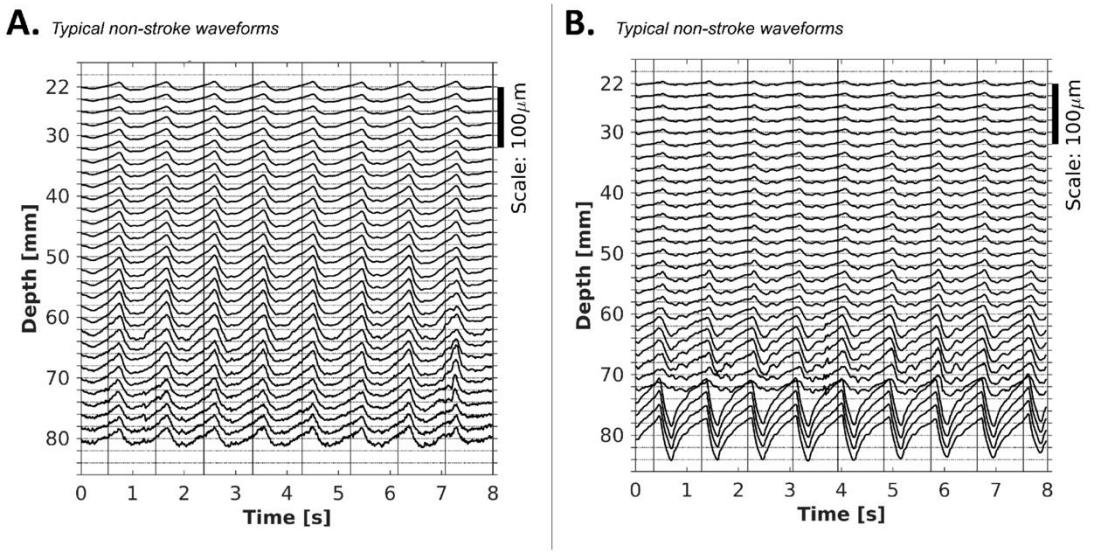

Figure 1-3 Normal BTP signals without strokes [1]. Panel A shows consistent waveform patterns across different depths, while panel B shows slight variations in waveform patterns among different depths.

doi:10.6342/NTU202403075

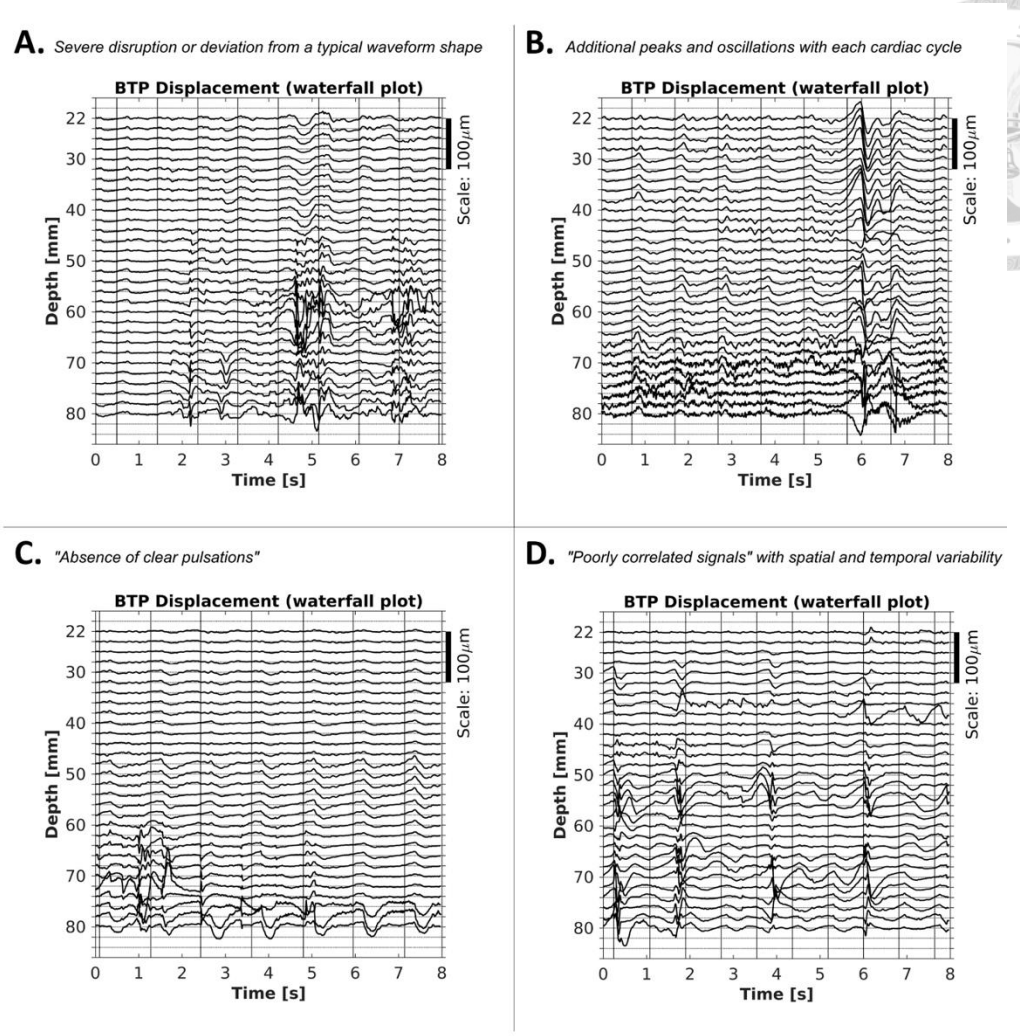

Figure 1-4 Typical stroke BTP signals [1] Panel A: Dramatic perturbation or departure from a regular waveform configuration. Panel B: Unlike single peaks observed in non-stroke waveforms, there are several additional peaks and oscillations after pulsations. Panel C: "The lack of discernible heartbeats." Panel D: "Inadequately correlated signals," which exhibit temporal and spatial heterogeneity [1]

1.2.3 Mathematical Model

The mathematical literature review will explain how the governing equations are shown in the next chapter. Using a unique application of a one-dimensional, fully dynamic, multiple-network poroelastic (MPET) formulation, the study examined the effects of intentionally produced aqueductal stenosis and atresia. [6]. Aqueductal stenosis and

doi:10.6342/NTU202403075

atresia refer to the narrowing and complete blockage of the cerebrospinal fluid flow pathway in the brain. A high-pressure arterial network (a), a lower-pressure arteriole/capillary network (c), an interstitial fluid (ISF)/CSF network (e), and a venous network (v) are the components that make up the quadruple MPET system. [17].

Eq. (1) of equilibrium is needed to represent elastic deformation in a poroelastic media, whereas Eq. (2) of Darcy's law is needed to characterize fluid flow. Mass conservation needs to be taken into account as well. [6].

$$\sigma_{ij} = 2G\epsilon_{ij} + \lambda\epsilon_{kk}\delta_{ij} - \sum_{A=a,e,c,v} \alpha^A p^A \delta_{ij} \quad (1)$$

$$\boldsymbol{q}_A = -\frac{k_A}{\mu_A}(\nabla p^A), A = a, e, c, v \quad (2)$$

In the MPET framework, the initial governing equation of motion for a unit volume is provided by:

$$\sigma_{ij,j} + \left[\sum_{A=a,e,c,v} (n^A(\rho^A - \rho_s) + \rho_s)\right](b_i - \ddot{u}_i) - \sum_{A=a,e,c,v} \rho^A\left(\dot{w}_i^A + w_j^A w_{i,j}^A\right) = 0 \quad (3)$$

where $\sigma_{ij,j}$ is the stress within the solid matrix. The mean displacement of elements forming the solid matrix is described by u_i. w_i is the ratio of fluid flow to cross sectional area and $\sum_{a=1}^{A} n^a\rho^a + (1-n)\rho_s$ is the total density of the system, ρ_s is the solid density and $\sum_{a=1}^{A} n^a$ is the total porosity of all the individual fluid networks.

The equation determining the momentum of each distinct fluid network is the second governing equation of motion:

doi:10.6342/NTU202403075

$$p_i^A - R_i^A - \rho^A(b_i - \ddot{u}_i) - \frac{\rho_A}{n^A}\left(\dot{w}_i^A + w_j^A w_{i,j}^A\right) = 0 \quad (4)$$

Where R_i^A is the viscous drag force (Zien-kiewicz et al., 1999) using Darcy's seepage rule. The fluid phase's flow conservation is provided by:

$$S_\varepsilon^A \dot{p}^A + \alpha^A \dot{\varepsilon}_{ii} + w_{i,i}^A + \frac{1}{\rho^A}\dot{\rho}^A = \sum_{A=a,e,c,v} \overbrace{\omega_{ij}(p_j - p_i)}^{\hat{s}_{ij}} \quad (5)$$

where $\dot{\varepsilon}_{ii}$ is the rate at which the strain inside the solid matrix changes. α^A represents the fluid network's Biot parameter of the fluid network in question. The right-hand side possesses either source ($\hat{s}_{ij} > 0$) or sink ($\hat{s}_{ij} < 0$) densities. $\boldsymbol{q}$ represents the fluid flux vector. The fluid phase continuity equations from Eq. (5) contain the sum of all flows inside a compartment ($\hat{s}_{ij}$). A hydrostatic pressure gradient drives the transfer, and the transfer coefficient ω_{ij} scales the flow from network j to network i. By deleting w_A from Eq. (4) as done by Tully and Ventilos (2011), one can then focus on the primary variables u and p. Using Darcy's seepage law (Zienkiewiz et al., 1999) and Eq. (4), one therefore obtains:

$$w_i^A = k_{ij}^A p_i^A - k_{ij}^A \rho^A\left(b_j - \ddot{u}_j\right) \quad (6)$$

The anisotropic permeability coefficient is defined as k_{ij}^A. This value is substituted with a single k^A constant (which here should be supposedly) if isotropy is assumed. Substituting Eq. (6) into Eq. (5), one therefore will be:

$$S_\varepsilon^a \dot{p}^a + \alpha^a \varepsilon_{ii} + \left[k_{ij}^a p_i^a - k_{ij}^a \rho^a\left(b_j - \ddot{u}_j\right)\right] - \sum_{A=a,e,c,v} \hat{s}_{ij} = 0 \quad (7)$$

doi:10.6342/NTU202403075

The final form of the system yields by combining Eq. (1) and Eq(3) :

$$\nabla \cdot \boldsymbol{\sigma} - \sum_{A=a,e,c,v} \alpha^A \nabla p^A + \rho_s(\boldsymbol{b} - \ddot{\boldsymbol{u}}) = 0 \quad (8)$$

$$S_\varepsilon^A \dot{p^A} + \alpha^A \dot{\boldsymbol{\varepsilon}} + \nabla \cdot [k^A \cdot \rho^A(\boldsymbol{b} - \ddot{\boldsymbol{u}}) - k^A \cdot \nabla \rho^A] - \sum_{A=a,e,c,v} \hat{s}_{ij} = 0 \quad (9)$$

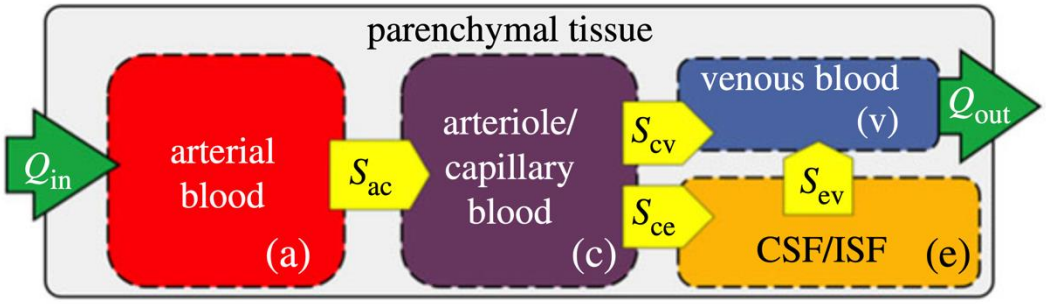

Figure 1-5 The four compartment MPET model. There is directional transfer between (a) and (c), (c) and (v), (c) and (e), and lastly (e) and (v), but the CSF and the artery network are cut off to flow. [13].

Another study also applied the MPET model. By reviewing this paper, the MPET model employs the displacement of parenchymal tissue (u) and the pore pressures of the four fluid compartments (pa, pc, pe, pv) as the primary variables in the governing equations. [13]. As shown in Figure 1 5. The governing equations of Figure 1 5 are listed below(Eq. (10) – Eq. (14))

$$G\nabla^2 \boldsymbol{u} + (G + \lambda)\nabla_\varepsilon = \alpha_a \nabla p_a + \alpha_c \nabla p_c + \alpha_e \nabla p_e + \alpha_v \nabla p_v \quad (10)$$

$$S_a \frac{\partial p_a}{\partial t} + \alpha_a \frac{\partial \varepsilon}{\partial t} = \frac{\mathbf{k}_a}{\mu_a} \nabla^2 p_a + \hat{s}_{c \to a} \quad (11)$$

$$S_c \frac{\partial p_c}{\partial t} + \alpha_c \frac{\partial \varepsilon}{\partial t} = \frac{\mathbf{k}_c}{\mu_c} \nabla^2 p_c + (\hat{s}_{c \to a} + \hat{s}_{e \to c} + \hat{s}_{v \to c}) \quad (12)$$

$$S_e \frac{\partial p_e}{\partial t} + \alpha_e \frac{\partial \varepsilon}{\partial t} = \frac{\mathbf{k}_e}{\mu_e} \nabla^2 p_e + (\hat{s}_{c \to e} + \hat{s}_{v \to e}) \quad (13)$$

doi:10.6342/NTU202403075

$$S_v \frac{\partial \mathrm{p_v}}{\partial \mathrm{t}} + \alpha_\mathrm{v} \frac{\partial \varepsilon}{\partial \mathrm{t}} = \frac{\mathbf{k}_\mathrm{v}}{\mu_v} \nabla^2 \mathrm{p_v} + (\hat{\mathrm{s}}_{c \to v} + \hat{\mathrm{s}}_{e \to v}) \quad (14)$$

The equilibrium equation representing the momentum balance in the porous media is Eq. (10); the Lame's constant is λ, and the shear modulus is G.; ε the dilatational strain; α_i the Biot-Willis coefficient for each fluid compartment that satisfies $\phi \leq \alpha_a + \alpha_c + \alpha_e + \alpha_v \leq 1$, where ϕ is the total porosity. The mass balance is described by the continuity Eq.(11) through Eq.(14). S_i stands for specific storage, which is a measurement of each fluid compartment's released fluid volume per unit pressure in the control volume under constant strain; For an isotropic media, $\mathbf{k}_\mathrm{i} = \mathrm{k_i}\mathbf{I}$ where I is the unit tensor and ki is a constant, represents the permeability tensor for each of the four fluid compartments. The viscosity of each fluid compartment is represented by μ_i.. The $\hat{s}$ terms in equation (11)-(14) define the spatially varying source ($\hat{s}_{ij} > 0$) or sink ($\hat{s}_{ij} < 0$) densities (rat of fluid transfer between networks).

1.3 **Aims and Scope**

The aim is to construct a mathematical model and fit it to specific data. The mathematical model is similar to those discussed in previous literature reviews. Transcranial tissue Doppler (TCTD) ultrasound is used to measure the displacement of brain tissue caused by cardiac pulsations to obtain data, along with corresponding blood pressure measurements. By acquiring synchronised ultrasound signals of displacement

doi:10.6342/NTU202403075

and blood pressure and applying Fourier transformation, the transfer function can be derived by dividing the displacement signal by the blood pressure signal. This transfer function is the data needed to fit with the mathematical model.

After the literature review, here are going to elaborate the scope. This study will then introduce the materials and methods used in Chapter 2, including how to build Model 1 and Model 2 using different governing equations, how to obtain and process the experimental data and the methods for fitting the models to the data. Chapter 3 will analyse the results from Chapter 2 and make relevant comparisons. Finally, this study will summarise the findings and discuss potential directions for future research.

doi:10.6342/NTU202403075

2 Materials and Methods

This chapter will introduce two mathematical models used here, which include how the governing equation arises and how to analyse the governing equations. Also, it will show the procedure of acquiring data from healthy volunteers, including the machine used and the way to process data. Finally, after trying to fit the model to the data, the results are shown in the next chapter.

2.1 Mathematical Model

2.1.1 Governing Equations:

This study hypothesizes that brain tissue can be represented as a coupled solid-fluid system with a single fluid compartment. This assumption leads to the established governing equations for such a system:

$$G\nabla^2 w + \frac{G}{1-2v}\nabla(\nabla.\mathrm{w}) - \alpha\nabla.pI = \rho_s \frac{\partial^2 w}{\partial t^2} \tag{15}$$

$$\nabla.\left(\frac{\kappa}{\mu}\nabla p\right) = \frac{\partial}{\partial t}\left(\alpha\nabla.\mathrm{w} + \frac{p}{Q}\right) \tag{16}$$

In this model, termed Model 1, the solid component is characterised as a linear, isotropic material with density ρ, shear modulus G, and Poisson's ratio ν. The fluid component adheres to Darcy's law, described by permeability κ and viscosity μ, with the Biot-

doi:10.6342/NTU202403075

Willis coefficient represented by α and specific storage denoted as Q. The fluid experiences pressure p, while the solid undergoes displacement w. These formulations have been supported by several studies, including those by Tully et al. (2009), Chou et al. (2016). Vardakis et al. (2016), and Guo et al. (2018). It is important to recognise that this biomechanical model of brain tissue simplifies the actual complexity of a nonlinear, viscoelastic, and highly anisotropic material, which will be revisited in the next paragraph. Additionally, using a single fluid compartment is a simplification for the ease of this analysis.

As this study assumes brain tissue to be a linear, isotropic material and considering a single fluid compartment, the computational process is facilitated. The model does not fully capture the complex, nonlinear, viscoelastic, and anisotropic nature of actual brain tissue. However, such assumptions might lead to underestimating or overestimating the proper mechanical response, affecting the accuracy of results.

To streamline the equations, which is essential here due to the experimental data being available only as a function of radial distance, the initial assumption is spherical symmetry. This means that spatial variations are limited to the radial direction. Consequently, by setting $\mathrm{w} = w\hat{\mathbf{r}}$, the equations yield:

$$\frac{G}{r^2}\frac{\partial}{\partial r}\left(r^2\frac{\partial w}{\partial r}\right)+\frac{G}{1-2v}\frac{\partial}{\partial r}\left(\frac{1}{r^2}\frac{\partial(r^2 w)}{\partial r}\right)-\frac{\alpha}{r^2}=\rho_s\frac{\partial^2 w}{\partial t^2} \tag{17}$$

doi:10.6342/NTU202403075

$$\frac{k}{\mu}\frac{1}{r^2}\frac{\partial}{\partial r}\left(r^2\frac{\partial p}{\partial r}\right)=\alpha\frac{1}{r^2}\frac{\partial(r^2w)}{\partial r}+\frac{1}{Q}\frac{\partial p}{\partial t} \tag{18}$$

given the linearity of the problem, the solution is separated into two parts: a steady-state component and an oscillating component:

$$w(r,t)=w_0(r)+\widehat{w}_1(r)e^{i\omega t} \tag{19}$$

$$p(r,t)=p_0(r)+\hat{p}_1(r)e^{i\omega t} \tag{20}$$

given the periodic nature of the cardiac pulsations, the model can be simplified significantly by assuming a sinusoidal form for the oscillating components. Additionally, the linearity of the model allows us to analyze different harmonics of the pulsations independently.

The attention is centered on the oscillating component, since it is the one measured in situ. Inserting the trial solution into the two governing equations produces:

$$\frac{d^2\widehat{w}_1}{dr^2}+\frac{2}{r}\frac{d\widehat{w}_1}{dr}+\widehat{w}_1\left[\frac{\rho_s\omega^2}{E}\frac{(1+\nu)(1-2\nu)}{(1-\nu)}-\frac{1}{(1-\nu)}\frac{1}{r^2}\right]=\frac{\alpha(1+\nu)(1-2\nu)}{E(1-\nu)}\frac{1}{r^2}\frac{d(r^2\hat{p}_1)}{dr} \tag{21}$$

$$\frac{d^2\hat{p}_1}{dr^2}+\frac{2}{r}\frac{d\hat{p}_1}{dr}-\hat{p}_1\left(\frac{i\omega\mu}{\kappa Q}\right)=\left(\frac{\alpha i\omega\mu}{\kappa}\right)\frac{1}{r^2}\frac{d(r^2\widehat{w}_1)}{dr} \tag{22}$$

where shear modulus has been replaced by Young' s modulus using the relationship:

$$G=\frac{E}{2(1+\nu)} \tag{23}$$

Note that the governing equations are second order in both pressure and displacement. Hence, four boundary conditions are required.

doi:10.6342/NTU202403075

2.1.2 **Nondimensionalization**

While this model is considerably simplified, it still incorporates a significant number of parameters (eight), which presents a challenge in terms of fitting from the available experimental data. Therefore, to delve deeper into the model's behaviour, all variables are non-dimensionalized by using characteristic values for radius, displacement, and pressure, represented as $r' = \frac{r}{R_c}$, $\mathrm{w}' = \frac{\hat{w}_1}{w_c}$, $and\ p' = \frac{\hat{p}_1}{p_c}$.

$$\frac{d^2\mathrm{w}'}{dr'^2} + \frac{2}{r'}\frac{d\mathrm{w}'}{dr'} + \mathrm{w}'\left[\pi_1 \frac{(1+\nu)(1-2\nu)}{(1-\nu)} - \frac{1}{(1-\nu)}\frac{1}{r'^2}\right] = \pi_4 \frac{(1+\nu)(1-2\nu)}{(1-\nu)}\frac{1}{rr'^2}\frac{d\left(r'^2 p'\right)}{dr'} \tag{24}$$

$$\frac{d^2p'}{dr'^2} + \frac{2}{r'}\frac{dp'}{dr'} - p'(i\pi_2) = i\pi_3 \frac{1}{r'^2}\frac{d\left(r'^2\mathrm{w}'\right)}{dr'} \tag{25}$$

The resulting equations are thus governed by just four non-dimensional groups:

$$\pi_1 = \frac{\rho_s \omega^2 R_c^2}{E} \tag{26}$$

$$\pi_2 = \frac{\omega \mu R_c^2}{\kappa Q} \tag{27}$$

$$\pi_3 = \frac{\alpha \omega \mu R_c w_c}{\kappa p_c} \tag{28}$$

$$pi_4 = \frac{\alpha R_c p_c}{E w_c} \tag{29}$$

Together with the Poisson's ratio (thus reducing the number of degrees of freedom to five). It is worth noting that two of these are of order 1, and two are much larger, which indicates that a boundary layer is probably found in the solution, or these values might be considerably reduced when aligned with experimental data. A boundary layer is a

doi:10.6342/NTU202403075

region where dependent variables would change rapidly. When having two second-order terms among the non-dimensional groups suggests that the behaviour of the system changes significantly over a small region. When aligning the model with experimental data, the second-order terms might be reduced because the experimental data might show behaviour different from the model prediction.

Four boundary conditions are necessary for this model. At the brain surface, zero displacements (i.e., the skull remains static) and unit non-dimensional amplitude pressure (i.e., this study references everything to this pulsation, which is defined as the characteristic pressure) at the brain surface. At the inner surface, where $\boldsymbol{r'} = \boldsymbol{\delta}$,, there is assumed zero fluid flux (i.e., no blood flows into the ventricles), and a mixed boundary condition for displacement (i.e., the stiffness of the ventricles is finite, so that neither Neumann nor Dirichlet boundary conditions are appropriate). The final boundary condition is expressed as follows:

$$\frac{dw'}{dr'} + kw' = 0 \tag{30}$$

It's worth noting that incorporating compliance effects is straightforward by making the non-dimensional stiffness $\boldsymbol{k}$ complex (although do not adopt this here to keep the parameter set as small as possible). Since the parameter $\boldsymbol{k}$ is difficult to estimate, an initial setting value of 1 implies an approximately linear variation. There are, thus, in total, seven non-dimensional parameters that govern the behaviour of the brain tissue

doi:10.6342/NTU202403075

in response to cardiac pulsations. The governing equations can be numerically solved easily using a boundary value solver with the given boundary conditions.

2.1.3 Cartesian form

It first examined the governing equations in the Cartesian form to move forward, assuming a variation with depth (x) and neglecting the effects of curvature. This simplification allows us to present the equations more straightforwardly and facilitates the comparison of results across different coordinate systems. Applying the same method as previously, the governing equations yield:

$$\frac{d^2w'}{dx'^2} + \pi_1 \frac{(1+\nu)(1-2\nu)}{(1-\nu)} w' = \pi_4 \frac{(1+\nu)(1-2\nu)}{(1-\nu)} \frac{dp'}{dx'} \tag{31}$$

$$\frac{d^2w'}{dx'} - p'(i\pi_2) = i\pi_3 \frac{dw'}{dx'} \tag{32}$$

Note that the governing equations can convert this into a fourth-order governing equation for either displacement or pressure. Additionally, the effects of Poisson's ratio can be incorporated into the corresponding non-dimensional groups, thus reducing the number of free parameters. For illustrative purposes, numerical solutions for both coordinate systems are plotted in Figure 2-1 using the values given in Table 2-1.

Although the overall trend for displacement magnitudes is consistent, some variations are observed (pressure curves exhibit similar behaviours), with significant differences in phase variations. The presence of a boundary layer is also clearly evident in the

doi:10.6342/NTU202403075

solution. Here are going to revisit these behaviors later after a more detailed examination of the experimental data; however, given the notable differences, this study will adopt the spherical solution here to enhance accuracy.

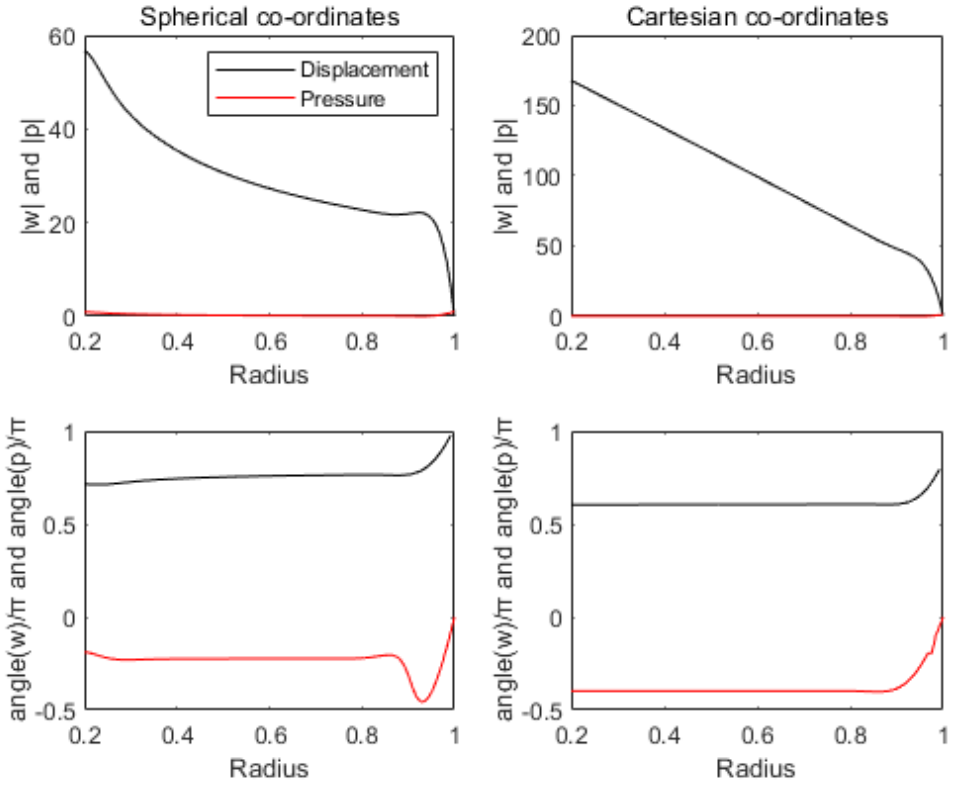

Figure 2-1 Magnitude and phase of displacement and pressure as function of depth, using parameter values in Table 2-1 Typical values of model parameters and their types and sources

2.1.4 Revised Model

Here introduce this revised model for reasons which will be explained in the next Chapter. For these reasons, Model 1 is re-evaluated in detail to separate blood pressure into its arterial and venous compartments. By distinguishing between these two pressures. As a result, the equations were restructured into the following three

doi:10.6342/NTU202403075

formulations, which are more physiologically reasonable:

$$\frac{d^2w}{dr^2}+\frac{2}{r}\frac{dw}{dr}+\left(\frac{\rho_s\omega^2}{E}\frac{(1+\nu)(1-2\nu)}{1-\nu}-\frac{1}{(1-\nu)}\frac{1}{r}\right)w = \frac{(1-2\nu)(1+\nu)}{(1-\nu)E}\left(\alpha_a\frac{dp_a}{dr}+\frac{2\alpha_a}{r}p_a+\alpha_v\frac{dp_v}{dr}+\frac{2\alpha_v}{r}p_v\right) \quad (33)$$

$$(i\omega)\alpha_a\frac{dw_1}{dr}+\frac{1}{Q_a}(i\omega)p_{a1}-\frac{\kappa_a}{\mu_a}\left(\frac{2}{r}\frac{dp_{a1}}{dr}+\frac{d^2p_{a1}}{dr^2}\right)= -\beta(p_{a1}-p_{v1}) \quad (34)$$

$$(i\omega)\alpha_v\frac{dw_1}{dr}+\frac{1}{Q_a}(i\omega)p_{v1}-\frac{\kappa_v}{\mu_v}\left(\frac{2}{r}\frac{dp_{v1}}{dr}+\frac{d^2p_{v1}}{dr^2}\right)= \beta(p_{a1}-p_{v1}) \quad (35)$$

Here, β is the coupling coefficient. The coupling coefficient β indicates the strength of interaction or coupling between two different physical quantities. Here, it describes the fluid transfer between different vascular compartments. Specifically, β represents the rate of fluid flow from one vascular compartment to another due to pressure differences. Therefore, there should be β_{av} representing a couple coefficient between the artery and venous. The way to estimate β_{av} is shown in Eq. (36) from the study [7]:

$$\beta_{av}=\frac{\bar{f}_G}{\bar{\phi}_a(\bar{p}_a-\bar{p}_v)} \quad (36)$$

Note that the equations can be simplified.αa is equal to αv, and Q_a is equal to Q_v exactly. The venous $\frac{\kappa}{\mu}$ is nearly three times of the arterial $\frac{\kappa}{\mu}$ according to a recent study by Jozsa et al. (2020). So the magnitude of them will be set as $3\frac{\kappa}{\mu}$, $\frac{\kappa}{\mu}$, respectively. The nondimensionalization is the same as before: $r'=\frac{r}{R_c}$, $w'=\frac{\hat{w}_1}{w_c}$, $and\ p_a{}'=\frac{\hat{p}_{a1}}{p_c}$, $p_v{}'=\frac{\hat{p}_{v1}}{p_c}$. Then, the equations yield:

doi:10.6342/NTU202403075

$$\frac{d^2w'}{dr'^2}+\frac{2}{r'}\frac{dw'}{dr'}+\left(\frac{\rho_s\omega^2R_c^2}{E}\frac{(1+\nu)(1-2\nu)}{1-\nu}-\frac{1}{1-\nu}\frac{1}{r'^2}\right)w' = \frac{(1+\nu)(1-2\nu)R_cp_c\alpha}{(1-\nu)Ew_c}\left(\frac{dp_a'}{dr'}+\frac{2}{r'}p_a+\frac{dp_v'}{dr'}+\frac{2}{r'}p_v'\right) \quad (37)$$

$$-\frac{d^2p_a'}{dr'^2}-\frac{2}{r'}\frac{dp_a'}{dr'}+i\frac{\omega\mu R_c^2}{\kappa Q}p_{a1}'+i\frac{\alpha\omega\mu R_cw_c}{\kappa p_c}\frac{1}{r'^2}\frac{dw_1'}{dr'} = -\frac{\mu R_c^2\beta}{\kappa}(p_{a1}-p_{v1}) \quad (38)$$

$$-\frac{d^2p_v'}{dr'^2}-\frac{2}{r'}\frac{dp_v'}{dr'}+i\frac{\omega\mu R_c^2}{\kappa Q}p_{v1}'+i\frac{\alpha\omega\mu R_cw_c}{\kappa p_c}\frac{1}{r'^2}\frac{dw_1'}{dr'} = \frac{\mu R_c^2\beta}{3\kappa}(p_{a1}-p_{v1}) \quad (39)$$

Here are going to use non-dimensional groups like before. The three equations would become:

$$\frac{d^2w'}{dr'^2}+\frac{2}{r'}\frac{dw'}{dr'}+\left(\pi_1\frac{(1+\nu)(1-2\nu)}{1-\nu}-\frac{1}{1-\nu}\frac{1}{r'^2}\right)w' = \pi_4\frac{(1+\nu)(1-2\nu)}{(1-\nu)}\left(\frac{dp_a'}{dr'}+\frac{2}{r'}p_a+\frac{dp_v'}{dr'}+\frac{2}{r'}p_v'\right) \quad (40)$$

$$-\frac{d^2p_a'}{dr'^2}-\frac{2}{r'}\frac{dp_a'}{dr'}+i\pi_2p_{a1}'+i\pi_3\frac{1}{r'^2}\frac{dw_1'}{dr'} = -\pi_5(p_{a1}-p_{v1}) \quad (41)$$

$$-\frac{d^2p_v'}{dr'^2}-\frac{2}{r'}\frac{dp_v'}{dr'}+i\pi_2p_{v1}'+i\pi_3\frac{1}{r'^2}\frac{dw_1'}{dr'} = \frac{\pi_1}{3}(p_{a1}-p_{v1}) \quad (42)$$

The resulting equations are thus governed by such five non-dimensional groups:

$$\pi_1=\frac{\rho_s\omega^2R_c^2}{E} \quad (43)$$

$$\pi_2=\frac{\omega\mu R_c^2}{\kappa Q} \quad (44)$$

$$\pi_3=\frac{\alpha\omega\mu R_cw_c}{\kappa p_c} \quad (45)$$

$$\pi_4=\frac{\alpha R_cp_c}{Ew_c} \quad (46)$$

$$\pi_5=-\frac{\mu R_c^2\beta}{\kappa} \quad (47)$$

Those are thus the five non-dimensional parameters this study are going to fit in this new model.

doi:10.6342/NTU202403075

2.2 Data Acquisition

This section will introduce the methods of getting data and processing data. Turner P et al. (2020) collected brain tissue pulsation data from 33 distinct depths within the brains of volunteers using an adapted Spencer Technologies (Seattle, WA, USA) transcranial Doppler (TCD) system with a 2-MHz transducer. TCTD data were gathered for each participant from four different probe positions: through the left and right temporal windows, and from the forehead above the center of each eyebrow. Each ultrasound recording was 8s long, providing tissue motion data from 33 overlapping 3-mm sample depths spaced 2mm apart, depths ranging from 22-86 mm.

2.2.1 Acquisition Methods

Turner P et al. (2020) use Transcranial tissue Doppler (TCTD) ultrasound to estimate BTPs in 20 volunteers, both at rest and during a lower-leg-raise manoeuvre designed to elevate blood pressure (BP) temporarily. This facilitated the time-series analysis of continuous data under a repeated measures study design, in which subjects served as their own controls. Synchronous physiological measurements for BP, forehead BTP, and end-tidal CO_2 ($EtCO_2$) were acquired using Brain Tissue Velocimetry (Brain TV), a TCTD data acquisition prototype (Nihon Kohden, Japan), equipped with a 2 MHz single-element TCD probe (Spencer Technologies, MA, USA). BTP measurements

doi:10.6342/NTU202403075

were recorded from the right side of the forehead of each participant using a custom-made elasticated headband to hold the probe.[2]

Synchronous BP readings are acquired by using a finger-cuff Finometer system (Finapres Medical System B.V., Enschede,NL) attached to the left wrist of each participant, with a cuff of the appropriate size positioned around the left middle finger. As CO_2 is known to impact vasodilation and cerebral autoregulatory responses, capnography measurements of $EtCO_2$ were obtained using an OLG-3800 CO2 monitor (Nihon Kohden, Japan), connected to a nasal cannula. A 3-lead electrocardiogram (ECG) (Lifescope monitor, Nihon Kohden, Japan) recorded the timing of ECG wave R-R intervals to allow adjustment for HR and beat-to-beat analysis of time-series data. All physiological monitoring data were recorded using a sampling rate of 500 Hz.[2]

Participants sat upright with their eyes closed. In each acquisition period, a 1-minute baseline recording at rest, a 1-minute recording of three repeated lower-leg-raise manoeuvres, and 1 minute for recovery were included. Figure 2-2 summarises the physiological measurement set up for the lower-leg-raise experiment. The elasticated headband was set on the head with a 2MHz TCD ultrasound probe for detecting brain tissue pulsation(BTP). Synchronous physiological measurements for BP, forehead BTP, and end-tidal CO_2($EtCO_2$) were acquired using Brain Tissue Velocimetry (Brain TV).

doi:10.6342/NTU202403075

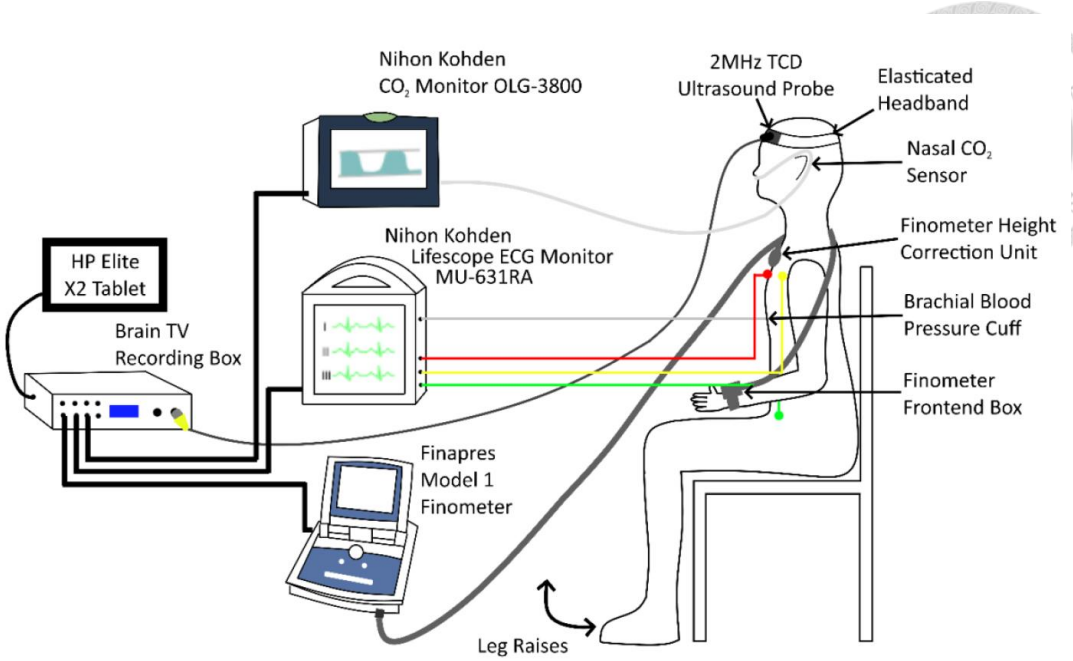

Figure 2-2 Equipment used in data acquisition [2]

2.2.2 Data Processing

After the data have been recorded, some processing is needed to get into a form that can be directly compared with the model predictions. Processing initially segments the time series of blood pressure and tissue displacement into individual cardiac cycles by identifying peaks in the arterial blood pressure trace. It is performed by using the function called “findpeaks” in MATLAB with the condition of appropriate minimum peak height and minimum peak distance.

doi:10.6342/NTU202403075

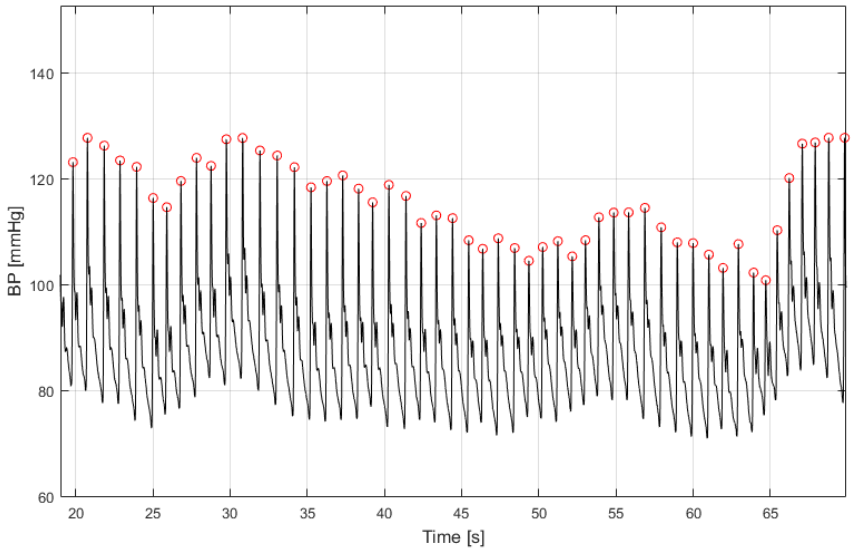

Figure 2-3 A typical subject of arterial blood pressure (ABP) time series, peaks marked in red circles, each interval between circles representing a cardiac cycle.

As shown in Figure 2-4, the data is divided into individual cardiac cycles and interpolated linearly onto a regular cardiac cycle. For clarity, only a single cardiac cycle is shown in Figure 2-4.

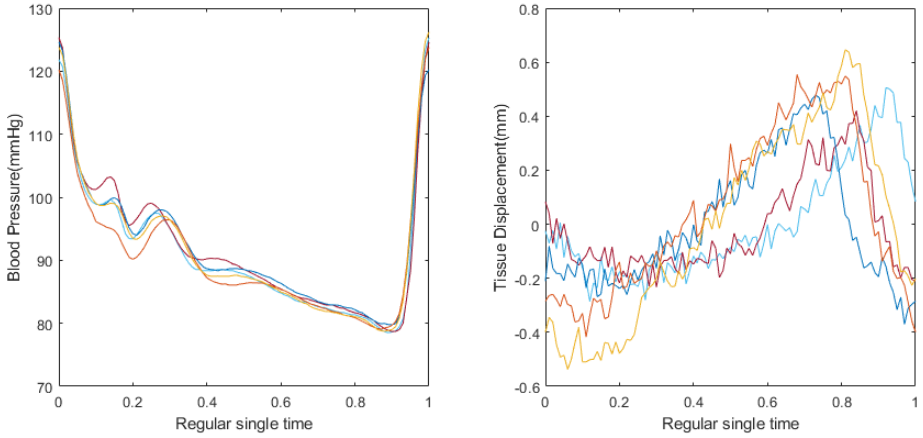

Figure 2-4 Typical subjects of pressure and displacement in single regular cardiac cycle

Since everything is referenced to the blood pulsations, the displacement and the pressure are directly comparable. Thus, the transfer function between arterial blood pressure and displacement is calculated by using the complex Fourier transform at the

doi:10.6342/NTU202403075

cardiac frequency and then averaging the complex coefficients over all the cardiac cycles. The final transfer function is obtained by dividing the complex coefficient of displacement by the complex coefficient of pressure. Thus, there is a time-averaged transfer function at each depth.

Data from 20 participants were utilised to generate individual gain and phase trajectories. Although participant responses varied significantly, a consistent trend was observed: amplitudes were minimal at the surface, increased with depth, and diminished beyond a specific depth. This trend corresponds to the latter section of the proposed model, as depicted in Figure 2-5 Extraction of the average gains and phase.

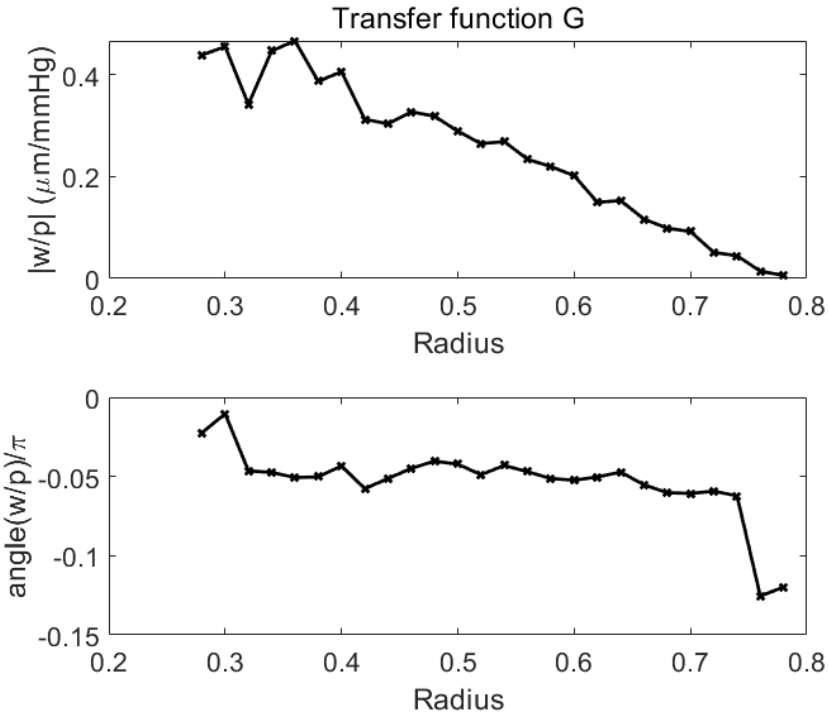

Figure 2-5 Extraction of the average gains and phase

doi:10.6342/NTU202403075

2.3 Model Fitting

This chapter will introduce the software and coding language used and the parameters of the mathematical model.

2.3.1 Methods and Tools

After processing the data, here are prepared to initiate the model fitting procedure. For this purpose, the function that will be utilised is the 'fminsearch' function in MATLAB, which is used for unconstrained optimisation. It finds the minimum of a scalar function of several variables starting at an initial estimate by using the Nelder-Mead simplex algorithm. The algorithm iteratively adjusts a set of points in the function's domain. It doesn't require gradient information and works by reflecting, expanding, and contracting these points to locate the minimum. This function is particularly useful for nonlinear optimisation problems where the objective function, which in this case is the governing equation, is not easily differentiable. The chosen loss function for optimisation is the sum of absolute deviations, which will assist in identifying the optimal curve fit. This method can be combined with fminsearch to get the best curve.

2.3.2 Parameters Setting

Here are going to consider the probable magnitudes of the four non-dimensional groups

doi:10.6342/NTU202403075

before examining numerical solutions. The model parameters' typical values are given in Table 1 below. The first three can be measured directly from the time series data, and the typical values can be obtained from the table. The next set of four values is used widely in the literature and is likely to show little variation from these values (the poroelastic constant $\boldsymbol{\alpha}$ is set to be equal to one under the assumption that the material is fully saturated); However, the last five are much less well-known. Thus, it will be started by adopting the values used by previous authors. These are thus the five parameter values that are aimed to investigate here.

Parameter	Value	Type	Sources
ω	O(2π)	Measured	Experimental data (see below)
p_c	O(1000)Pa	Measured	
w_c	O(100)μm	Measured	
α	1	Well-known	Standard values widely used in literature
δ	0.2	Well-known	
ρ_s	977kg/m^3	Well-known	
R_c	0.1m	Well-known	
κ/μ	3.75×10-8m^{3}s/kg	Not Well-known	Values taken from Vardakis et al., Guo et al., and Chou et al.
ν	0.35	Not well-known	
E	583N/m^2	Not well-known	
κ	1	Not well-known	
Q	3.33×10^{3}kg/m.s	Not well-known	

doi:10.6342/NTU202403075

Table 2-1 Typical values of model parameters and their types and sources

Then, the four non-dimensional values can be calculated using the typical values above. The initial results are shown in Table 2.

Parameter	Typical value
π_1	0.677
π_2	503
π_3	1.67
π_4	1.72×103

Table 2-2 Baseline values of non-dimensional groups

For the second model, the values of new parameters are also referenced from [7].

Parameter	Value and units	Source
$\bar{f}_G$	50ml/100g	Kety and Schmidt [8]
$\bar{\phi}_a$	0.0102	Tio et al. [9]; Ito et al.[10]
$\bar{\phi}_c$	0.0034	
$\bar{\phi}_v$	0.0204	
$\bar{p}_a$	80mmHg	Vovenko [12]; Lipowsky[11]
$\bar{p}_c$	35mmHg	
$\bar{p}_v$	20mmHg	

Table 2-3 Baseline values of model parameters and sources and/or calculations for blood flow [7].

2.4 Conclusion

This study introduces two mathematical models to investigate the mechanical properties of brain tissue, particularly how it responds to pulsations caused by cardiac

doi:10.6342/NTU202403075

pulsations. This chapter elaborated on the development of the two models, data acquisition methods from healthy volunteers, and the subsequent data processing steps. TCTD is used to measure brain tissue displacement and corresponding blood pressure. Fourier transformation is used to analyse the data, fitting the models to this data using MATLAB's 'fminsearch' function.

doi:10.6342/NTU202403075

3 Results and Discussions

This chapter will present the results obtained from the various methods described in the previous chapter and provide detailed analyses and visual representations for each method, allowing for a clear comparison of their performance under different conditions. After presenting the results, this chapter will summarise the key findings, highlighting the strengths and weaknesses of each method. Finally, it will be discussed which method performs best overall, considering both quantitative results and qualitative factors like ease of implementation and computational requirements. This will help identify the most suitable method and suggest further research or improvement areas.

3.1 Fitting Results

This section contains four parts showing what difficulties are met and how fitting is performed. First, the difficulty showed that some of the estimated values are negative, whereas the mechanical properties cannot be negative. After solving this problem, the next problem is that fitting encountered unreasonable values that differ from the actual situation. Then, something unreasonable is found in the fitting process. However,

doi:10.6342/NTU202403075

reasonable values are attained in the last part.

3.1.1 Original Model Fitting

The model fitting of Model 1 was initiated here, and the results from the initial fitting are illustrated in the figure below, with all the initial values coming from Table 2-1. The curve appears smooth. However, upon examining the parameters π_1 to π_4, there are negative values show up, as shown in Table 3-1, which is physically implausible as these dimensionless parameters cannot be negative.

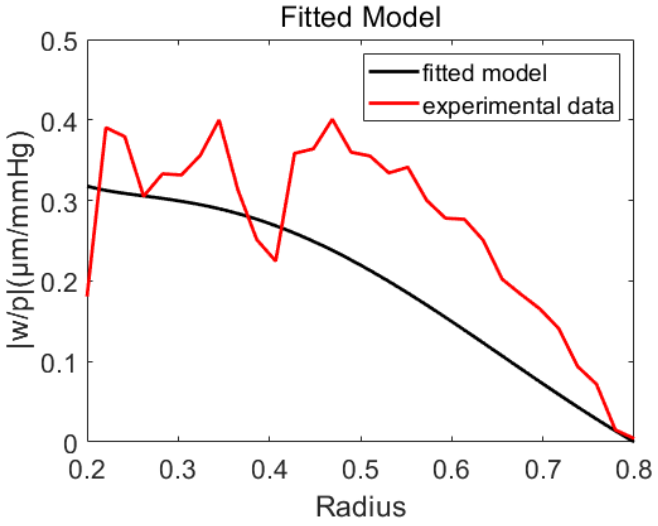

Figure 3-1 Original model fitting

π_1	35.35
π_2	-2.982×10^6
π_3	1.112×10^6.
π_4	2.62

Table 3-1 Original model fitting of π_1 to π_4

doi:10.6342/NTU202403075

3.1.2 Logarithmic Transformation of The Parameters

The next step is to apply a logarithmic transformation to the parameters. Specifically, before feeding the parameters π_1 through π_4 into the function, they are converted to their logarithmic equivalents, $\log(\pi_1)$ to $\log(\pi_4)$. Within the function itself, π_1 to π_4 are replaced with $\exp(\pi_1)$ to $\exp(\pi_4)$. The main advantage of this approach is that the model effectively fits the logarithm of πs, which ensures that even if a negative value is fitted during the optimisation process, taking the exponential of this negative value will result in a positive outcome. This maintains the inherent positivity of the parameters while offering the added benefit of greater numerical stability.

By utilising this method, all parameters now yield positive values, indicating progress towards the correct solution. The next step involves calculating the following key parameters: ν (Poisson's ratio), E (Young's modulus), Q (specific storage), and κ/μ (permeability over viscosity). However, solving all four parameters simultaneously proved challenging. Notably, Poisson's ratio is known to generally fall within a range of 0.35 to 0.5, a narrow interval with values that are very close but not identical, while other parameters are not well known and have a very large range. Besides, other parameters do not have a specific value or clearly defined range in existing literature. Consequently, the decision is made to iterate through this range with Poisson's ratio

doi:10.6342/NTU202403075

values between 0.35 and 0.49, adjusting each increment by 0.01. This iterative approach simplifies the task by reducing the number of unknowns, leaving only three parameters to be solved for each value of Poisson's ratio.

Moreover, this strategy provides a more controlled and systematic approach to parameter estimation. By carefully constraining its range, the stability and reliability of the remaining parameter estimates are enhanced. This methodology thus enables a more refined analysis of Young's modulus, specific storage, and permeability over viscosity, allowing for accurate modelling and improved insights into the underlying mechanics.

Now, let's recall the equations of π_1 to π_4：

$$\pi_1 = \frac{\rho_s \omega^2 R_c^2}{E} \tag{26}$$

$$\pi_2 = \frac{\omega \mu R_c^2}{\kappa Q} \tag{27}$$

$$\pi_3 = \frac{\alpha \omega \mu R_c w_c}{\kappa p_c} \tag{28}$$

$$\pi_4 = \frac{\alpha R_c p_c}{E w_c} \tag{29}$$

Because of knowing all the parameter values except E, κ/μ and Q, they can be calculated by using the equations for π1, π3 and π_2, respectively.

$$E = \frac{\rho_s \omega^2 R_c^2}{\pi_1} \tag{48}$$

$$\frac{\kappa}{\mu} = \frac{\alpha \omega R_c w_c}{\pi_3 p_c} \tag{49}$$

$$Q = \frac{\omega \mu R_c^2}{\kappa \pi_2} \tag{50}$$

doi:10.6342/NTU202403075

The results corresponding to each individual value of ν are shown in Table 3-2.

v	E(Pa)	Q(kg/m.s)	$\frac{\kappa}{\mu}$(m^{3}s/kg)	Loss(μm/mmHg)
0.35	9.26	Inf	4.01×10^{-10}	5.430
0.36	8.80	1.05×10^{115}	4.00×10^{-10}	5.420
0.38	7.79	Inf	3.92×10^{-10}	5.402
0.39	7.27	2.85×10^{113}	3.90×10^{-10}	5.393
0.41	6.15	Inf	3.83×10^{-10}	5.372
0.42	5.56	1.87×10^{13}	3.79×10^{-10}	5.362
0.44	4.32	Inf	3.71×10^{-10}	5.340
0.45	3.67	6.06×10^{17}	3.67×10^{-10}	5.327
0.47	2.28	Inf	3.58×10^{-10}	5.303
0.48	1.54	5.46×10^{268}	3.53×10^{-10}	5.290
0.49	0.79	1.53×10^{217}	3.48×10^{-10}	5.277

Table 3-2 Results of parameters for corresponding Poisson's ratio, where Inf represents a value out of the range of the numerical solver.

Analysis encountered significant issues. One is that infinite results in specific storage (Q), which might mean the zero appears in the denominator during the fitting process. Another is when evaluating the model at specific values of Poisson's ratio, specifically 0.37, 0.40, 0.43, and 0.46. The Jacobian matrix, which is critical for understanding the system's sensitivity and ensuring the stability of numerical solutions, became singular at these values. The reason might be that the parameters form a redundant set or inappropriate initial values were used. A singular Jacobian matrix implies that the

doi:10.6342/NTU202403075

determinant of the matrix is zero, indicating that the system of equations is either overdetermined or underdetermined at these points. This situation leads to computational difficulties, such as the inability to accurately invert the matrix, which is necessary for the optimisation and fitting processes.

The singularity of the Jacobian matrix suggests that small changes in the input parameters could result in disproportionately large changes in the output, making the system highly unstable and unreliable. Therefore, to ensure the robustness and reliability of the model, the decision is made to skip the results for these specific values of Poisson's ratio. By doing so, the computational pitfalls associated with singular matrices were avoided, and the integrity of the fitting process was maintained.

Skipping these values, while necessary, also highlights the limitations of the current approach and suggests that further refinement of the model or alternative numerical techniques may be required to handle such cases more effectively in future studies. The precise reasons for this are not yet fully understood. The resulting fitting curves are shown in Figure 3-2. In order to observe the trend of the 3 parameters, they are plotted with respect to the Poisson's ratio, as shown in Figure 3-3.

doi:10.6342/NTU202403075

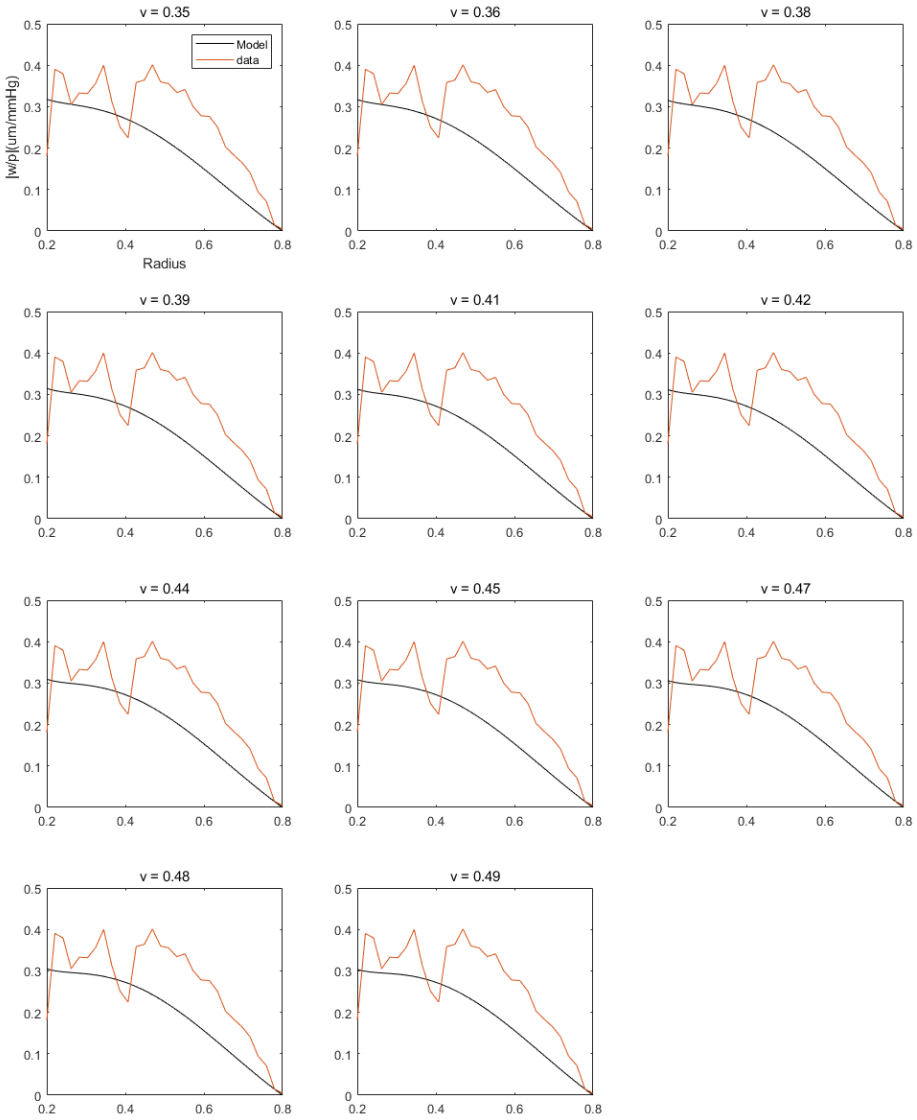

Figure 3-2 Fitted curves correspond to different Poisson's ratio, skipping singular Jacobian matrix values.

doi:10.6342/NTU202403075

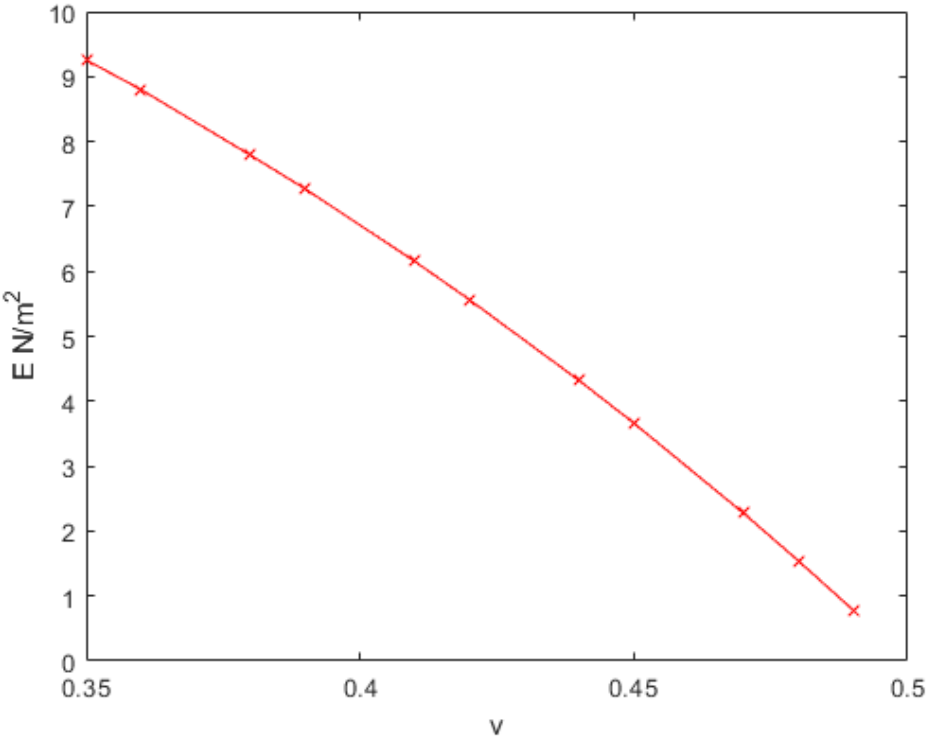

Figure 3-3 Young's modulus variation with different Poisson's ratio

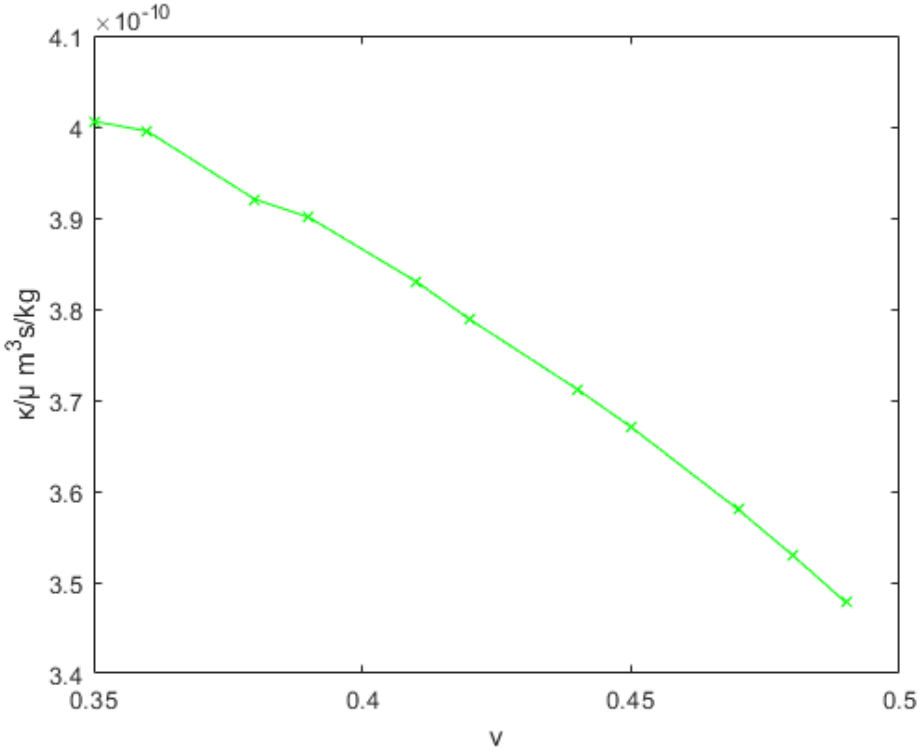

Figure 3-4 Permeability over viscosity variation with different Poisson's ratio

doi:10.6342/NTU202403075

3.1.3 Fitting with the New Model

By applying the new model and comparing it to Model 1, there is no longer the singular Jacobian matrix. Each Poisson's ratio has results for its corresponding parameters. Additionally, it is found that the values are surprisingly stable, which means the fluctuation of each parameter is less or around the order of 10^2. The results of different Poisson's ratios by using fminsearch are shown in Table 3-3:

ν	E (Pa)	Q(kg/m.s)	$\frac{\kappa}{\mu}$(m^{3}s/kg)	Loss(μm/mmHg)
0.35	2.442×10^{5}	7.492×10^{5}	9.325×10^{-9}	4.721
0.36	1.326×10^{3}	1.052×10^{6}	1.892×10^{-9}	4.708
0.37	2.735×10^{3}	1.056×10^{6}	2.164×10^{-9}	4.695
0.38	1.223×10^{3}	1.481×10^{4}	3.152×10^{-7}	4.680
0.39	682.8	9.800×10^{5}	2.324×10^{-9}	4.666
0.4	433.1	1.640×10^{6}	2.881×10^{-11}	4.652
0.41	1.961×10^{4}	3.810×10^{5}	1.163×10^{-8}	4.637
0.42	739.7	1.268×10^{4}	1.833×10^{-8}	4.622
0.43	727.5	1.373×10^{4}	1.712×10^{-8}	4.606
0.44	628.4	9546	2.383×10^{-8}	4.590
0.45	1.149×10^{4}	2.241×10^{5}	2.046×10^{-8}	4.574
0.46	427.3	11.10	4.417×10^{-5}	4.557
0.47	1127	4.945×10^{5}	1.244×10^{-8}	4.540
0.48	789.5	3.542×10^{5}	1.596×10^{-8}	4.524

doi:10.6342/NTU202403075

0.49	2834	2.315×10^{4}	2.084×10^{-7}	4.504

Table 3-3 Fitted results corresponding to different Poisson's ratio

The corresponding fitting curves are shown in Figure 3-5. The loss function is shown in Figure 3-6 . It can be observed that the fitting curves are smooth for all values of Poisson's ratio, which means that the fitting appears to work well. Besides, the values are also very reasonable. It was observed that Young's modulus values are mostly around one to two thousand Pa, the specific storage values fall between 10^{5} and 10^{6} kg/m.s, and the permeability over viscosity values are approximately 10^{-8} $m^{3}s/kg$. These values are close to the initial estimates provided in the literature, and the loss is less than 5 to all magnitudes of Poisson's ratio. Because of that, the resulting model appears to fit the data very well.

doi:10.6342/NTU202403075

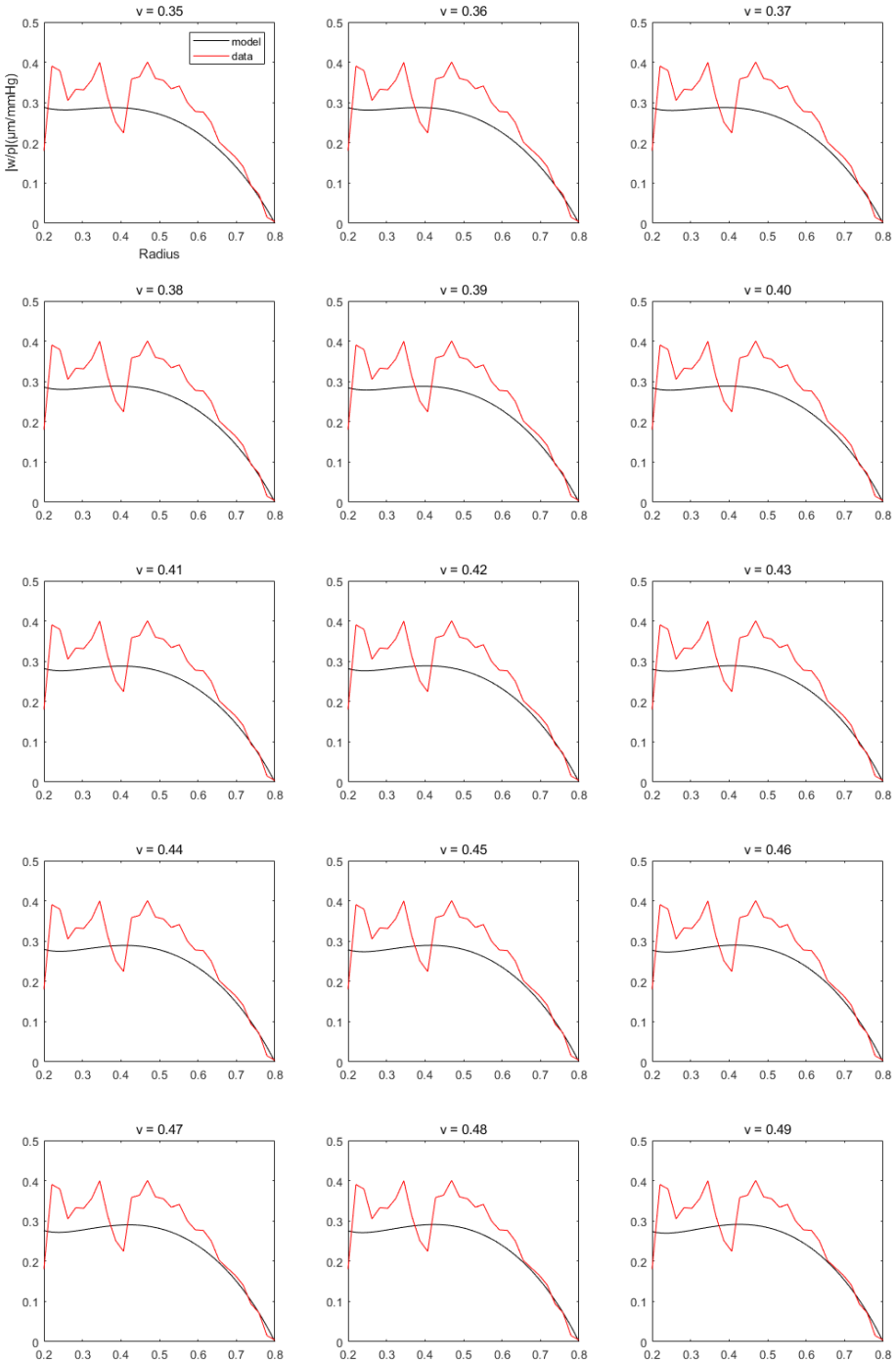

Figure 3-5 Fitted curves corresponding to different Poisson's ratios

doi:10.6342/NTU202403075

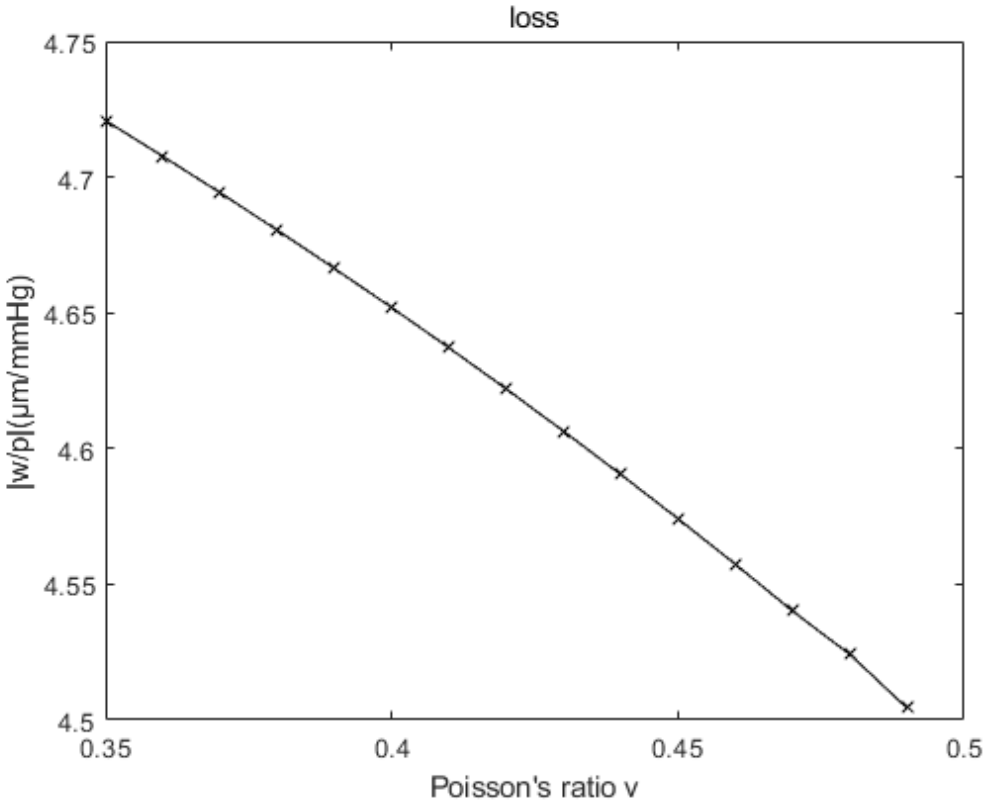

Figure 3-6 Loss function of Model 2

Several sets of results that are not so unreasonable are chosen for further studies. These results have been taken back to the model but given different results compared to the one in the last time fitting. For example, the fitting results at Poisson's ratio at 0.49 are shown in Table 3-4. The corresponding fitting curve is shown in Figure 3-7.

ν	E (Pa)	Q(kg/m.s)	$\frac{\kappa}{\mu}$ (m^3s/kg)
0.49	2834	2.315×10^{4}	2.084×10^{-7}

Table 3-4 fitted results at 0.49 of Poisson's ratio

doi:10.6342/NTU202403075

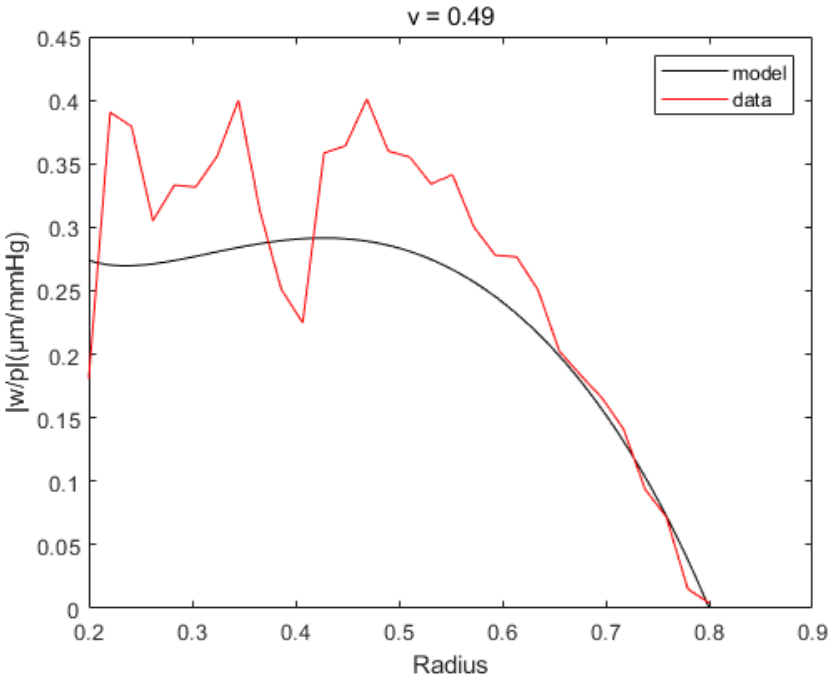

Figure 3-7 fitting results at 0.49 of Poisson's ratio

However, when these values are taken back to the model, which means the initiated values from Table 2-1 Typical values of model parameters and their types and sources become the values in Table 3-4, the outcome is shown in Figure 3-8. It is totally different from Figure 3-7, which means there are problems during the fitting process. To put it more simply, for example, we solved an equation, but when we substituted the solution back into the equation, we found that the original equation did not hold.

doi:10.6342/NTU202403075

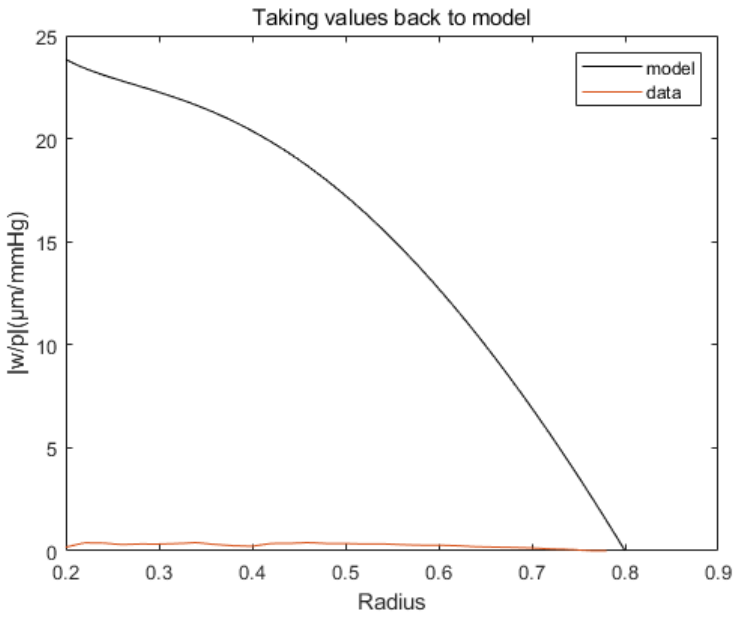

Figure 3-8 Taking values back to the model

After checking the fitting process, the problem showed up. Firstly, the non-dimensional parameters that are fitted are π1 to π5, and then Young's modulus, specific storage, and permeability over viscosity are calculated by those non-dimensional parameters. Here, recalling Eq. (43) to Eq. (47) again, it is easy to find that Young's modulus E can be calculated by Eq. (43), Specific storage can be calculated by Eq (44)., and permeability over viscosity can be calculated by Eq (45). The equations after transformation are shown in Eq. (48)-Eq. (50). Now three equations are used, but there are still two equations left, Eq(46) and Eq. (47). It is easy to find that the E calculated by Eq.(48) can't satisfy Eq. (46) . Thus, it needs to find new ways to solving this problem.

$$\pi_1 = \frac{\rho_s \omega^2 R_c^2}{E} \tag{43}$$

$$\pi_2 = \frac{\omega \mu R_c^2}{\kappa Q} \tag{44}$$

doi:10.6342/NTU202403075

$$\pi_3 = \frac{\alpha\omega\mu R_c w_c}{\kappa p_c} \tag{45}$$

$$\pi_4 = \frac{\alpha R_c p_c}{E w_c} \tag{46}$$

$$\pi_5 = -\frac{\mu R_c^2 \beta}{\kappa} \tag{47}$$

$$E = \frac{\rho_s \omega^2 R_c^2}{\pi_1} \tag{48}$$

$$\frac{\kappa}{\mu} = \frac{\alpha\omega R_c w_c}{\pi_3 p_c} \tag{49}$$

$$Q = \frac{\omega\mu R_c^2}{\kappa\pi_2} \tag{50}$$

3.1.4 Fitting the Original Three Parameters

One possible way is fitting the original three parameters directly so that there would be no problem between the five nondimensional parameters and the original three parameters of E, Q, and κ/μ. Thus, it is decided to fit the original three parameters, E, $\frac{\kappa}{\mu}$, and Q, in different Poisson's ratios ranging from 0.35 to 0.5, 0.01 apart.

The process of coding is quite easy, just changing the five nondimensional parameters to the three-dimensional parameters. The fitting results for each different value of Poisson's ratio are shown in Table 3-5, where these three parameters are fitted directly to the experimental data.

ν	E(Pa)	Q(kg/m.s)	$\frac{\kappa}{\mu}$(m^{3}s/kg)	Loss(μm/mmHg)
0.35	2246	3.027×10^{4}	4.87×10^{-13}	7.584
0.36	1389	1302	5.58×10^{-13}	7.584

doi:10.6342/NTU202403075

0.37	670.2	84.15	3.77×10^{-13}	6.674
0.38	1377	1278	6.51×10^{-13}	7.585
0.39	444.5	18.75	3.84×10^{-12}	7.585
0.4	1508	3693	6.08×10^{-13}	7.585
0.41	1108	1625	5.96×10^{-13}	7.586
0.42	695.0	61.07	3.83×10^{-12}	7.553
0.43	9.730	2.093×10^{6}	3.82×10^{-14}	7.584
0.44	1075	10.73	9.08×10^{-11}	7.516
0.45	4.460×10^{5}	68.63	7.96×10^{-5}	4.574
0.46	235.6	10.73	8.96×10^{-12}	7.518
0.47	179.2	10.92	8.65×10^{-12}	7.518
0.48	226.4	10.78	3.07×10^{-11}	7.519
0.49	8.949×10^{4}	1.409×10^{8}	2.06×10^{-4}	4.701

Table 3-5 fitting parameters to different Poisson's ratio

The corresponding curves are shown in Figure 3-9. Since the results look much worse than before, the three parameter results will not be shown.

doi:10.6342/NTU202403075

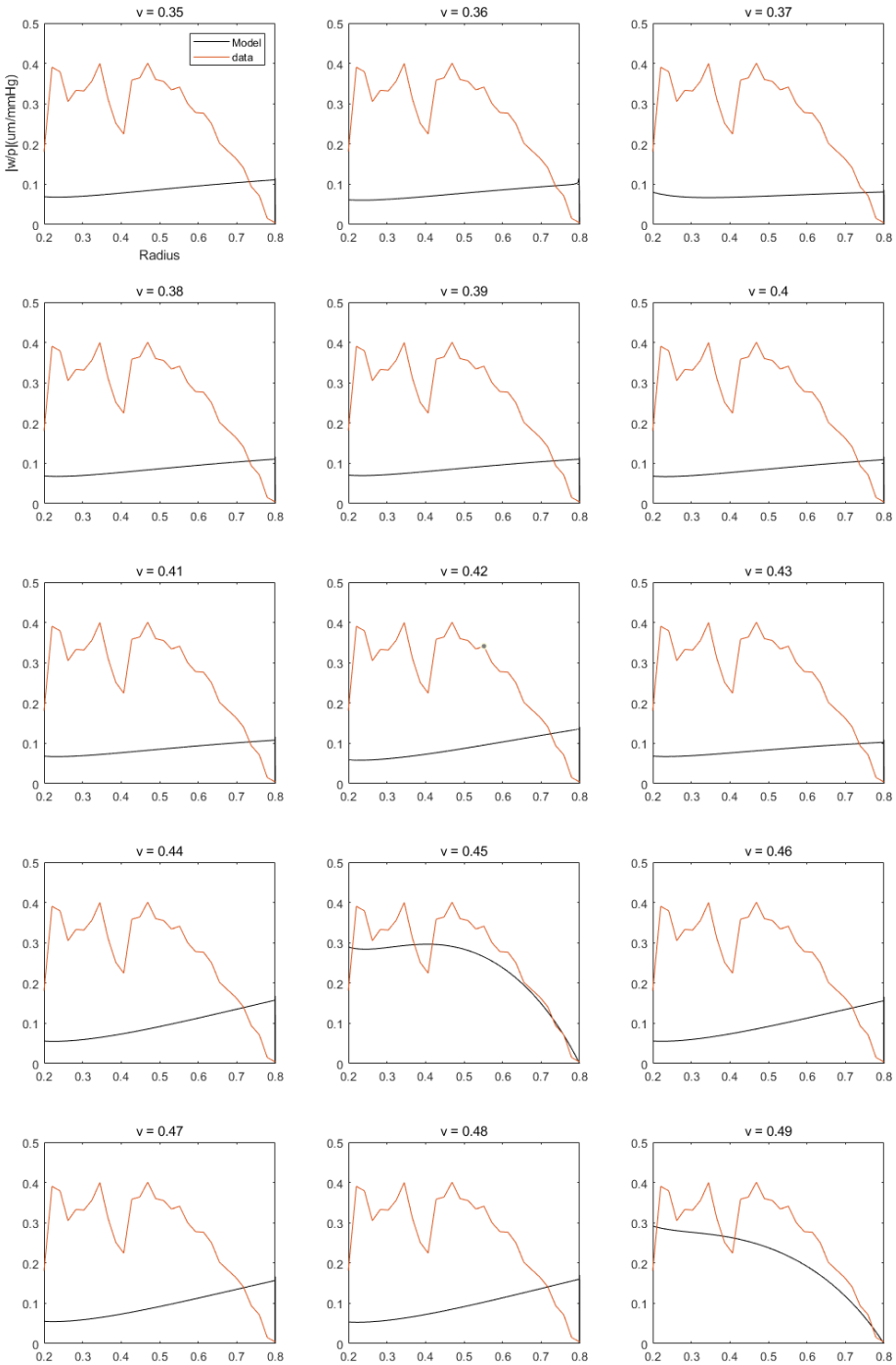

Figure 3-9 Fitting curves to different Poisson's ratio

The fitting values of parameters and curves are both unexpected. The values fluctuated

doi:10.6342/NTU202403075

widely. Young's modulus fluctuates from ten to nearly ninety thousand. Specific storage and the permeability over viscosity variants are even larger. The varianting range can attain the order of 10^{10}. However, since the curves show a relatively good fit at values of Poisson's ratio at 0.45 and 0.49, the decision was made to re-fit the model by using the results at these two values of Poisson's ratio as the starting condition to see if better results could be achieved.

The results using the values obtained at a Poisson's ratio of 0.45 as initial conditions are shown in Table 3-6

v	E(kPa)	Q(kg/m.s)	$\frac{\kappa}{\mu}$(m^3s/kg)	Loss(μm/mmHg)
0.35	1240	53.93	9.173×10^{-5}	7.282
0.36	1173	53.82	9.185×10^{-5}	7.280
0.37	1104	53.72	9.192×10^{-5}	7.278
0.38	1033	53.62	9.207×10^{-5}	7.276
0.39	960.4	53.52	9.202×10^{-5}	4.666
0.4	885.2	53.42	9.219×10^{-5}	4.652
0.41	807.8	53.32	9.226×10^{-5}	4.637
0.42	728.0	53.23	9.237×10^{-5}	4.622
0.43	645.9	53.13	9.233×10^{-5}	4.606
0.44	561.4	53.03	9.241×10^{-5}	4.591
0.45	474.4	52.93	9.250×10^{-5}	4.574
0.46	384.8	52.83	9.267×10^{-5}	4.557

doi:10.6342/NTU202403075

0.47	292.7	52.74	9.266×10^{-5}	4.540
0.48	197.9	52.64	9.270×10^{-5}	4.523
0.49	100.4	52.54	9.283×10^{-5}	4.504

Table 3-6 Fitted parameters to different Poisson's ratio

From Table 3-6, it can be seen that all three parameter values are more stable than before, Young's Modulus varying in a relatively small range of the order of 10, and specific storage and permeability over viscosity over even smaller ranges, less than an order of 10. However, Young's modulus still fluctuates quite widely compared to the other two parameters. The corresponding fitting curves are shown in Figure 3-8, fitting curves at different values of Poisson's ratio.

doi:10.6342/NTU202403075

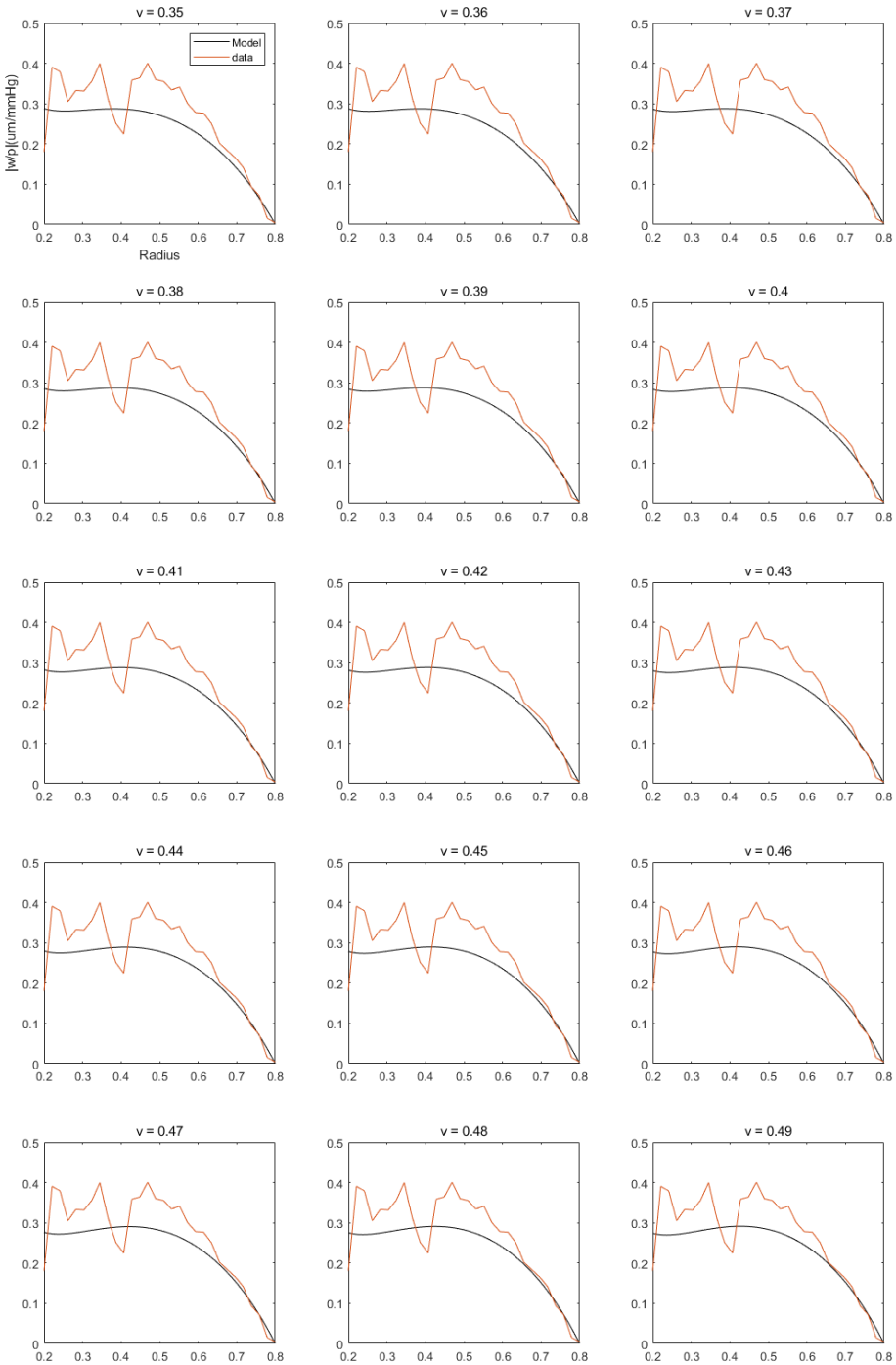

Figure 3-10 fitting curves to different Poisson's ratio

The curves look much better when compared to Figure 3-9. That means this set of

doi:10.6342/NTU202403075

parameters is more suitable for this model with improved initial values. Then, let us see the results of Poisson's at 0.49, as shown in Table 3-7.

v	E(kPa)	Q(kg/m.s)	$\frac{\kappa}{\mu}$(m^3s/kg)	Loss(μm/mmHg)
0.35	1240	53.93	9.173×10^{-5}	4.721
0.36	1173	53.83	9.186×10^{-5}	4.708
0.37	1104	53.72	9.194×10^{-5}	4.694
0.38	1033	53.62	9.207×10^{-5}	4.680
0.39	960.5	53.53	9.203×10^{-5}	4.666
0.4	885.3	53.43	9.214×10^{-5}	4.652
0.41	807.8	53.32	9.225×10^{-5}	4.637
0.42	728.0	53.23	9.237×10^{-5}	4.622
0.43	645.9	53.13	9.230×10^{-5}	4.606
0.44	561.4	53.03	9.243×10^{-5}	4.591
0.45	474.4	52.93	9.215×10^{-5}	4.574
0.46	384.8	52.833	9.266×10^{-5}	4.557
0.47	292.7	52.74	9.264×10^{-5}	4.540
0.48	197.9	52.64	9.277×10^{-5}	4.523
0.49	100.4	52.54	9.284×10^{-5}	4.504

Table 3-7 Fitting results corresponding to different Poisson's ratio

doi:10.6342/NTU202403075

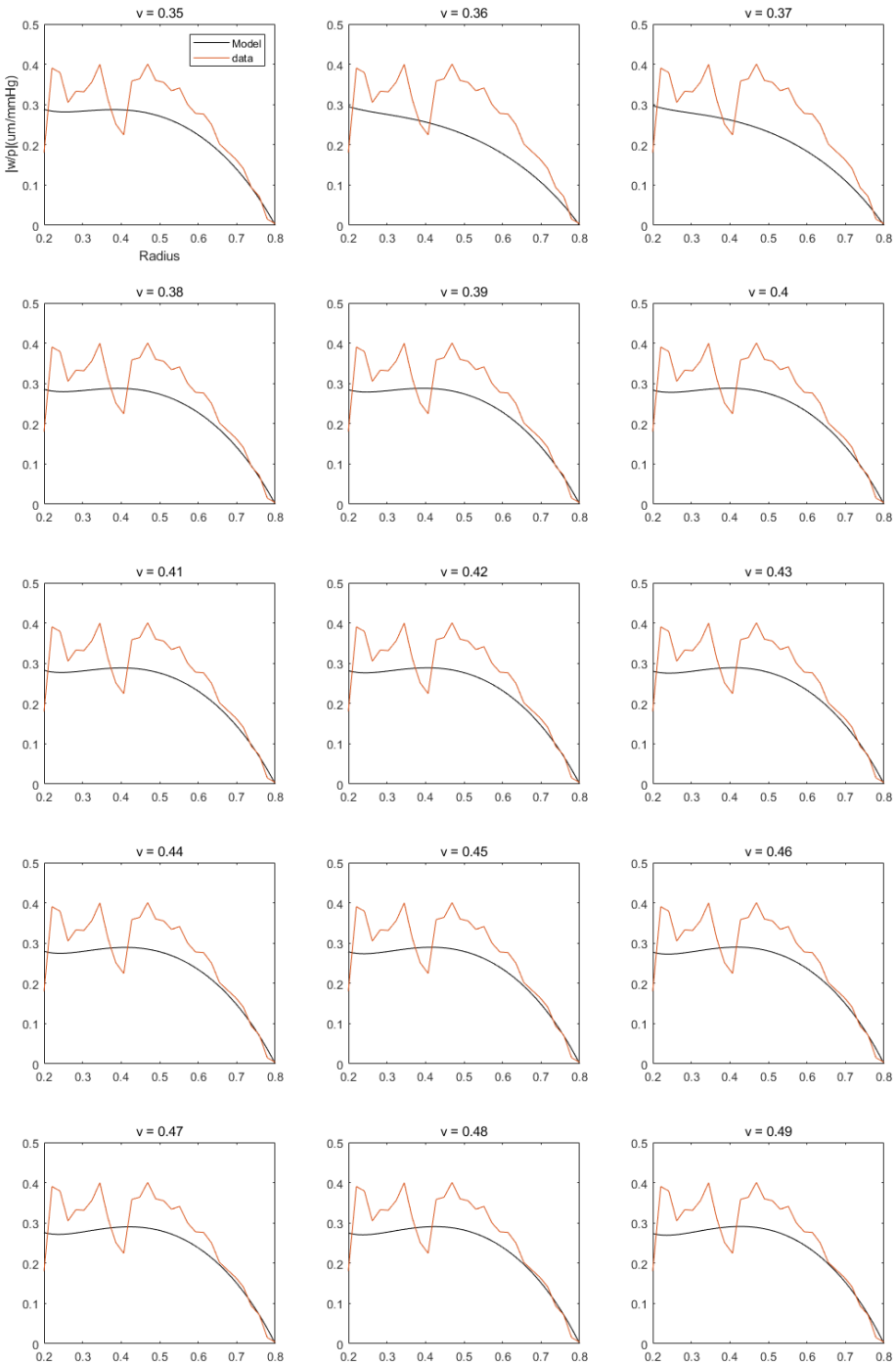

Figure 3-11 Fitting curves corresponding to different Poisson's ratio

The shape and trend of the curves again demonstrate a consistent alignment with the

doi:10.6342/NTU202403075

observed values. It also found that all the values of the parameter fluctuate minimally, as shown in Table 3-7. The corresponding figure is shown in Figure 3-11.

In summary, the results of Poisson's ratio at 0.45 and 0.49 show little fluctuation, and the fitting curves perform well, indicating that these are good initial values to use more generally. As shown in Table 3-8. However, it is worth noting that among these two sets of values, the only obvious difference is Young's modulus. Young's modulus at 0.45 of Poisson's ratio is nearly five times the value at 0.49, while the other two are almost the same.

ν	E (kPa)	Q(kg/m.s)	$\frac{\kappa}{\mu}$(m^{3}s/kg)	Loss(μm/mmHg)
0.45	474.4	52.93	9.250×10^{-5}	4.574
0.49	100.4	52.54	9.283×10^{-5}	4.504

Table 3-8 Results of parameters

3.2 Comparison and Discussion

This section will compare the fitting results of different models and discuss the significance and limitations of these results. It used two different models to fit the experimental data. The first included two equations, while the second model divided blood pressure into arterial and venous compartments, including three equations. Both models are mathematically compact and showed good fitting performance. The results are summarised in Table 3.8, including previous results at Poisson's ratio equals 0.49,

doi:10.6342/NTU202403075

since 0.49 of Poisson's ratio is more likely to be a reference value.

	E(Pa)	Q(kg/m.s)	$\kappa/\mu(m^3s/kg)$	Loss(μm/mmHg)
Model 1	0.7900	1.53×10^{217}	3.48×10^{-10}	5.277
Model 2	2834	2.315×10^{4}	2.084×10^{-7}	4.504
Model 2 (original 3 parameters)	8.949×10^{4}	1.409×10^{8}	2.060×10^{-4}	4.701
Model 2 (results at ν equals 0.49)	1.004×10^{5}	52.54	9.281×10^{-5}	4.504

Table 3-9 Comparison of each model at ν= 0.49

However, despite these results, there are still some issues in practical application. The first is fitted parameters. Model 1 initially fitted the parameters at a Poisson's ratio of 0.35 and obtained unrealistic parameter values. Then, 15 different Poisson's ratio values ranging from 0.35 to 0.49 were tried, but reasonable parameter values were still not found. In the second model, which distinguishes between arterial and venous blood pressures, which is closer to reality, the results are surprisingly stable. All the values of the parameters fall within a relatively small interval. However, when taking the result back to the model and trying to find a more accurate value of the parameters, the outcome curve did not correspond to the one during fitting. Then, the problem was found to be caused by the five non-dimensional parameters. Thus, it was decided to directly fit the original three parameters, skipping to fit the non-dimensional parameters. By doing this, the results can be taken back to the model and get the same curve as the

doi:10.6342/NTU202403075

fitting results.

According to the study done by Eneko Axpe et al. (2020). Young's modulus of brain tissue is typically shown to be in the range of a few hundred Pa to kPa [18]. Apparently, it differs significantly from the fitted results. The Poisson's ratio of brain tissue typically fell within the range of 0.35-0.5 [20]-[27]. According to a study of mathematical fitting done by Hinrichsen J et al. (2023), occasionally, the values of 0.45 and 0.49 were also used for fitting the Poisson's ratio [19]. To some extent, this is evidence to corroborate the idea that this study is going in the right direction. Although Young's modulus of fitting is not expected, the choice of Poisson's ratio still shows that this fitting has the potential to continue. However, there currently is no standard value for evaluating the fitting results as to whether they are right or not.

These issues indicate that there may be some unresolved problems between the mathematical models and the experimental data. Specifically, the model assumes that brain tissue is a linear, isotropic material, but in reality, brain tissue is nonlinear, viscoelastic, and highly anisotropic. Together with the subarachnoid space and the variable permeability of the brain, all may lead to a mismatch between the model and actual conditions. The sample size was limited to 20 healthy individuals, which may not represent the broader population. This small sample size might lead to biased results that do not reflect the general population's diversity.

doi:10.6342/NTU202403075

To improve the model's accuracy, more complex tissue models, such as viscoelastic or anisotropic properties, need to be considered, as well as the subarachnoid space and variable permeability, in particular between grey and white matter. Increasing the sample size and including individuals from different age groups and with various medical conditions will also help improve the model's applicability. While this study has made some preliminary achievements, further optimisation and validation are needed to estimate brain tissue's mechanical properties accurately. It must be considered more complex biomechanical properties and broader data sources to achieve improved results.

3.3 Conclusions

This section explores numerous methods to refine the model and improve the accuracy of calculations. This included adjusting various parameters, experimenting with different fitting algorithms, and applying several mathematical transformations. Despite rigorous testing and careful implementation, it faced consistent difficulties in obtaining reliable and consistent parameter values. While this study has not yet achieved the desired results, the efforts have highlighted the complexity of accurately modelling the mechanical properties of brain tissue. The challenges encountered underscore the need for further refining models and developing more advanced

doi:10.6342/NTU202403075

techniques. It remains optimistic that future studies can overcome these challenges and achieve the goals with continued research and the incorporation of more realistic tissue models and diverse datasets.

doi:10.6342/NTU202403075

4 Conclusions and Future Work

This study aimed to estimate the values of the mechanical properties of brain tissue from BTP recordings. Although estimating these robustly proved more challenging than expected, it is important to recognise that this is only a preliminary investigation. The results of this study lay the groundwork and exclude incorrect ways for future studies. With continued effort and exploration, more comprehensive and conclusive findings are anticipated in subsequent studies.

4.1 Summary of Findings

This study aimed to estimate the mechanical properties of brain tissue using a coupled solid-fluid mathematical model based on brain tissue pulsations (BTP). The key findings can be summarised as follows. The model performed well in fitting brain tissue responses to cardiac pulsations, demonstrating a high correlation with experimental data, as shown in Figure 3-2, Figure 3-5, Figure 3-10 and Figure 3-11. Despite significant variability among subjects, the model shows good performance at Poisson's ratio, which equals 0.45 and 0.49, which means that the properties of the brain appear to be close to incompressible. These two values are the same as those used by

doi:10.6342/NTU202403075

Hinrichsen J et al. (2023) in a previous study for fitting.

The initial values of Young's modulus estimated at 0.45 and 0.49 Poisson's ratio are 474.4kPa and 100.4kPa, respectively, which are very different from the values done by Axpe E et al. (2020). The specific storage and permeability over viscosity still do not have a standard value yet. Although what this study estimated may not be the correct answer, it does show a consistent behaviour in the last fitting of Model 2. However, due to large individual differences, the specific values of the mechanical properties remain uncertain. These results suggest that the proposed model has the potential for non-invasive assessment of brain mechanical properties, but that further optimisation and validation are needed.

4.2 Limitations

Although this study has considerable results on the mechanical properties of brain tissue, it is obvious that this study has limitations, including methodological limitations, data limitations, and scope limitations. Methodological limitations include that the model assumes linear, isotropic properties of brain tissue, which simplifies the tissue's complex, nonlinear, and anisotropic nature. Besides, the subarachnoid space and the variable permeability of the brain would also affect the fitting process. These should be considered in future work so that this study can attain an outcome that may be closer to

doi:10.6342/NTU202403075

reality.

Data limitations include the fact that the sample size was limited to 20 healthy individuals, which is enough to give a good start but not enough to go further. Obviously, these cannot represent the broader population. Scope limitations: The studies focused on healthy individuals and the applicability of the results to pathological conditions remains uncertain. More data, including both healthy individuals and patients, will need to be collected and applied for future research. Acknowledging these limitations is essential for accurately interpreting the results and guiding future research.

4.3 Future Work

Future work will focus on the problems that haven't been solved yet, extending current research and exploring new directions to enhance the model's robustness and applicability. One of the unresolved problems is the applicability and accuracy of the model. Although the multi-compartment nature of the blood flow is considered, it still has the potential to be more accurate, such as considering the variable permeability of the brain tissue. In addition, the model's performance can be assessed by applying it to different physiological and pathological states, such as brain trauma or neurodegenerative diseases. These will help validate and refine the model to ensure it accurately represents different states of brain health.

doi:10.6342/NTU202403075

For extending the research, this study can be expanded to include a larger and more diverse sample size. This should cover different age groups, genders, and individuals with varying medical histories. By doing this, the model may be able to reflect a wider range of human variability, improving its generalizability and accuracy. New research directions will include complex tissue models and will develop and integrate more tissue models that account for viscoelastic and anisotropic properties. These models should also consider the impact of the subarachnoid space and variable permeability on brain mechanics. Such enhancements will provide a more comprehensive understanding of brain tissue behaviour under different conditions.

Besides, future work also includes incorporating patient data to obtain and analyse data from patients with various neurological conditions to compare with the data from healthy individuals. Understanding the differences between healthy and pathological brain tissue properties will help clinical applications and model diagnostic capabilities. By solving these problems, this study will have a more comprehensive understanding of the properties of brain tissue, contributing more to clinical and physiology.

doi:10.6342/NTU202403075

5 Reference

[1] Ince J, Banahan C, Venturini S, Alharbi M, Turner P, Oura M, Beach KW, Robinson TG, Mistri AK, Lecchini-Visintini A, Minhas JS, Chung EML. Acute ischaemic stroke diagnosis using brain tissue pulsations. J Neurol Sci. 2020 Dec 15;419:117164. doi: 10.1016/j.jns.2020.117164. Epub 2020 Oct 3.

[2] S. Vidale, E. Agostoni, Prehospital stroke scales and large vessel occlusion: a systematic review, Acta Neurol. Scand. 138 (1) (2018) 24–31.

[3] Terem I, Dang L, Champagne A, Abderezaei J, Pionteck A, Almadan Z, Lydon AM, Kurt M, Scadeng M, Holdsworth SJ. 3D amplified MRI (aMRI). Magn Reson Med. 2021 Sep;86(3):1674-1686. doi: 10.1002/mrm.28797. Epub 2021 May 5.

[4] Turner P, Banahan C, Alharbi M, Ince J, Venturini S, Berger S, Bnini I, Campbell J, Beach KW, Horsfield M, Oura M, Lecchini-Visintini A, Chung EML. Brain Tissue Pulsation in Healthy Volunteers. Ultrasound Med Biol. 2020 Dec;46(12):3268-3278. doi: 10.1016/j.ultrasmedbio.2020.08.020. Epub 2020 Sep 24.

[5] J.C. Kucewicz, B. Dunmire, D.F. Leotta, H. Panagiotides, M. Paun, K.W. Beach, Functional tissue Pulsatility imaging of the brain during visual stimulation, Ultrasound Med. Biol. 33 (5) (2007) 681–690.

[6] Chou D, Vardakis JC, Guo L, Tully BJ, Ventikos Y. A fully dynamic multi-compartmental poroelastic system: Application to aqueductal stenosis. J Biomech. 2016 Jul 26;49(11):2306-2312. doi: 10.1016/j.jbiomech.2015.11.025. Epub 2015 Nov 28.

doi:10.6342/NTU202403075

[7] Moghadam ME, Baghal A, Payne S. Human whole-brain models of cerebral blood flow and oxygen transport. University of Oxford, Department of Biomedical Engineering.

[8] S.S. Kety, C.F. Schmidt, The nitrous oxide method for the quantitative determination of cerebral blood flow in man: theory, procedure and normal values, J. Clin. Invest. 27 (4) (1948) 476–483.

[9] H. Ito, I. Kanno, H. Iida, J. Hatazawa, E. Shimosegawa, H. Tamura, T. Okudera, Arterial fraction of cerebral blood volume in humans measured by positron emission tomography, Ann. Nucl. Med. 15 (2) (2001) 111–116, https://doi.org/10.1007/BF02988600.

[10] H. Ito, I. Kanno, H. Fukuda, Human cerebral circulation: positron emission tomography studies, Ann. Nucl. Med. 19 (2) (2005) 65–74, https://doi.org/10.1007/BF03027383.

[11] H.H. Lipowsky, Microvascular rheology and hemodynamics, Microcirculation 12(2005) 5–15.

[12] E. Vovenko, Distribution of oxygen tension on the surface of arterioles, capillaries and venules of brain cortex and in tissue in normoxia: an experimental study on rats, Pflugers Arch. 437 (1999) 617–623.

[13] Guo L, Vardakis JC, Lassila T, Mitolo M, Ravikumar N, Chou D, Lange M, Sarrami-Foroushani A, Tully BJ, Taylor ZA, Varma S, Venneri A, Frangi AF, Ventikos Y. Subject-specific multi-poroelastic model for exploring the risk factors associated with the early stages of Alzheimer's disease. Interface Focus. 2018;8(2):20170019. doi:10.1098/rsfs.2017.0019.

[14] Shao, Y.-H., & National Taiwan University Institute of Applied Mechanics. (2000). Non-invasive measurement of mechanical properties of peripheral arteries (I).

doi:10.6342/NTU202403075

Report of the National Science Council, Project No: NSC 89-2320-B-002-149 M08.

[15] Turner P, Banahan C, Alharbi M, Ince J, Venturini S, Berger S, Bnini I, Campbell J, Beach KW, Horsfield M, Oura M, Lecchini-Visintini A, Chung EML. Brain Tissue Pulsation in Healthy Volunteers. Ultrasound Med Biol. 2020;46(12):3268-3278. doi: 10.1016/j.ultrasmedbio.2020.08.020.

[16] Ince, J., Alharbi, M., Minhas, J.S., & Chung, E.M.L. (2019). Ultrasound measurement of brain tissue movement in humans: A systematic review. Ultrasound, 28(2), 70–81. doi: 10.1177/1742271X19894601.

[17] Tully, B., & Ventikos, Y. (2011). Cerebral water transport using multiple-network poroelastic theory: Application to normal pressure hydrocephalus. Journal of Fluid Mechanics, 667, 188-215. doi:10.1017/S0022112010004428.

[18] Axpe E, Orive G, Franze K, Appel EA. Towards brain-tissue-like biomaterials. Nat Commun. 2020 Jul 9;11(1):3423. doi: 10.1038/s41467-020-17245-x. PMID: 32647269; PMCID: PMC7347841.

[19] Hinrichsen J, Reiter N, Bräuer L, Paulsen F, Kaessmair S, Budday S. Inverse identification of region-specific hyperelastic material parameters for human brain tissue. Biomech Model Mechanobiol. 2023 Oct;22(5):1729-1749. doi: 10.1007/s10237-023-01739-w. Epub 2023 Sep 7. PMID: 37676609; PMCID: PMC10511383.

[20] Hosseini-Farid M, Ramzanpour M, McLean J, Ziejewski M, Karami G. A poro-hyper-viscoelastic rate-dependent constitutive modeling for the analysis of brain tissues. J Mech Behav Biomed Mater. 2020 Feb;102:103475. doi: 10.1016/j.jmbbm.2019.103475. Epub 2019 Oct 11. PMID: 31627069.

[21] M. Hosseini-Farid, M. Ramzanpour, M. Ziejewski, G. Karami, A compressible

doi:10.6342/NTU202403075

hyper-viscoelastic material constitutive model for human brain tissue and the identification of its parameters, Int. J. Non Linear Mech. 116 (2019)147–154 .

[22] Lee SJ, King MA, Sun J, Xie HK, Subhash G, Sarntinoranont M. Measurement of viscoelastic properties in multiple anatomical regions of acute rat brain tissue slices. J Mech Behav Biomed Mater. 2014 Jan;29:213-24. doi: 10.1016/j.jmbbm.2013.08.026. Epub 2013 Sep 9. PMID: 24099950; PMCID: PMC8011428.

[23] Nagashima T, Shirakuni T, Rapoport SI. A two-dimensional, finite element analysis of vasogenic brain edema. Neurol Med Chir (Tokyo). 1990 Jan;30(1):1-9. doi: 10.2176/nmc.30.1. PMID: 1694266.

[24] E. Comellas, S. Budday, J.P. Pelteret, G.A. Holzapfel, P. Steinmann, Modeling the porous and viscous responses of human brain tissue behavior, Comput. Methods Appl. Mech. Eng. 369 (2020) 113128 .

[25] Elkin BS, Ilankova A, Morrison B. Dynamic, regional mechanical properties of the porcine brain: indentation in the coronal plane. J Biomech Eng. 2011 Jul;133(7):071009. doi: 10.1115/1.4004494. PMID: 21823748.

[26] H. Kim, B.K. Min, D.H. Park, S. Hawi, B.J. Kim, Z. Czosnyka, M. Czosnyka, M.P. Sutcliffe, D.J. Kim, Porohyperelastic anatomical models for hydrocephalus and idiopathic intracranial hypertension, J. Neurosurg. 122 (6) (2015) 1330–1340 .

[27] Miller K, Chinzei K. Constitutive modelling of brain tissue: experiment and theory. J Biomech. 1997 Nov-Dec;30(11-12):1115-21. doi: 10.1016/s0021-9290(97)00092-4. PMID: 9456379.

[28] Payne SJ. Cerebral Blood Flow and Metabolism: A Quantitative Approach. World Scientific Publishing Co. Pte. Ltd., 2017.

doi:10.6342/NTU202403075